CHC22 clathrin membrane recruitment uses SNX5 in bipartite interaction with secretory tether p115

Joshua Greig[1], George T. Bates[1], Daowen I. Yin[1], Boris Simonetti[2], Peter J. Cullen[2], Frances M. Brodsky[1]*

*Corresponding author: f.brodsky@ucl.ac.uk

[1] Structural and Molecular Biology, Division of Bioscience, University College London, London, United Kingdom.

[2] School of Biochemistry, Faculty of Life Sciences, University of Bristol, Bristol, United Kingdom.

Condensed title: CHC22 clathrin membrane recruitment

Keywords: Clathrin, CHC22, SNX5, SNX6, SNX-BAR, p115, Terminal domain, ERGIC

Character count:

Summary statement

CHC22 clathrin uses a bipartite mechanism for recruitment to the early secretory pathway, where it targets the GLUT4 transporter to an insulin-responsive intracellular compartment. Localization requires binding to the ERGIC tether p115 through sorting nexin 5 interaction at the CHC22 C-terminus and directly via the CHC22 N-terminal domain.

Abstract

The two clathrin isoforms, CHC17 and CHC22, generate separate vesicles for intracellular transport. CHC17 mediates endocytosis and housekeeping membrane traffic in all cells. CHC22, expressed most highly in skeletal muscle, transports the glucose transporter GLUT4 from the endoplasmic-reticulum-to-Golgi intermediate compartment (ERGIC) to an intracellular GLUT4 storage compartment (GSC) from where GLUT4 is mobilized by insulin. Molecular determinants distinguishing the trafficking of CHC22 clathrin from CHC17 within the GLUT4 pathway are defined in this study. The C-terminal trimerization domain of CHC22, but not CHC17, directly binds SNX5, which also binds the ERGIC tether p115. SNX5, and the functionally redundant SNX6, are required for CHC22 localization independently of their participation in the endosomal ESCPE-1 complex. Both the SNX5-BAR domain and an isoform-specific patch on the CHC22 N-terminal domain separately mediate binding to p115, and both interactions are required for CHC22 recruitment. These indirect and direct interactions at each CHC22 terminus are required for GLUT4 traffic to the GSC, defining a dual mechanism regulating the function of CHC22 in glucose metabolism.

Introduction

The trafficking of membrane-bound proteins within cells requires vesicle-generating coat proteins that are spatially and temporally recruited to capture cargo at distinct intracellular locations. Clathrin coats mediate some of the major routes for such vesicular intracellular transport (Briant et al., 2020). Humans, along with several other vertebrate species, express two isoforms of the clathrin heavy chain, CHC17 and CHC22, named for the chromosome where they are encoded. CHC22 shares 85% sequence identity with CHC17 yet is distinct in both its recruitment profile and biochemical properties (Dannhauser et al., 2017).

CHC17 is the canonical form of clathrin that mediates receptor-mediated endocytosis and a range of intracellular trafficking pathways in all eukaryotic tissues (Briant et al., 2020). CHC22 clathrin, by contrast, has a narrower profile, being expressed most highly in skeletal muscle, and specializes in a subset of pathways and transported cargo (Dannhauser et al., 2017; Esk et al., 2010; Vassilopoulos et al., 2009). CHC22 is essential for trafficking the insulin-responsive glucose transporter GLUT4 to an intracellular storage compartment (GSC) where it awaits insulin-induced translocation to the cell surface (Camus et al., 2020; Esk et al., 2010; Hoshino et al., 2013; Vassilopoulos et al., 2009). Formation of the GSC and insulin-stimulated GLUT4 release is restricted to skeletal muscle and adipose tissue, with the former responsible for 70% of post-prandial glucose clearance in humans (Bogan, 2012; Gould et al., 2020; Leto and Saltiel, 2012). Malfunction of GLUT4 membrane traffic is one of the main features associated with Type 2 diabetes (Bogan, 2012). CHC22, which has variable expression in vertebrates, represents a key player in GLUT4 membrane traffic that operates in humans, but is missing from rodent models (Fumagalli et al., 2019). This study addresses the molecular basis for CHC22 specificity in GLUT4 traffic to identify mechanisms responsible for its specialized membrane recruitment to regulate human glucose metabolism.

The main mechanism by which CHC17 is recruited to intracellular membranes is via the binding of its N-terminal domain (TD) to a variety of adaptors that recognize both phosphoinositide and membrane-embedded cargo (Chen et al., 2020). These include both heterotetrametric adaptors AP1 and AP2, which recruit CHC17 to endosomes and the plasma membrane respectively, as well as the monomeric GGA adaptors that mediate protein sorting by clathrin-coated vesicles at endosomes and the *trans*-Golgi network (Briant et al., 2020). The CHC17 TD has a seven-bladed β-propeller structure and binds adaptors at four identified sites

(Lemmon and Traub, 2012). Equivalent binding sites on the CHC22 TD are predicted by sequence homology. However, CHC22 does not bind AP2, nor functions at the plasma membrane in receptor-mediated endocytosis, while demonstrating preferential binding to GGA2 compared to CHC17 (Dannhauser et al., 2017; Liu et al., 2001). This latter interaction, plus CHC22 binding to AP1, may account for CHC22 function in sorting GLUT4 from endosomes back to the GSC, following re-uptake from the plasma membrane by CHC17 after insulin-stimulated GLUT4 release (Gould et al., 2020). More recent work has shown that CHC22 is also a prerequisite for the initial establishment of the GSC, by transporting newly synthesized GLUT4 directly from the endoplasmic-reticulum-to-Golgi-intermediate compartment (ERGIC) to the GSC (Camus et al., 2020). In this ERGIC-to-GSC trafficking of GLUT4, CHC22 functions in a pathway where CHC17 has not been implicated. This function has been attributed to its specific participation in a sorting complex that includes the ERGIC tether protein p115, as well as insulin-responsive-amino peptidase (IRAP), which binds both p115 and GLUT4 (Camus et al., 2020; Hosaka et al., 2005).

How CHC22 interacts with different target membranes than those that recruit CHC17, and whether this involves the CHC22 TD, has not been established. In addition to CHC22's differential participation in a complex with p115, yeast-two-hybrid assays identified sorting nexin 5 (SNX5) as a protein that binds the C-terminal region of CHC22 but not CHC17 (Towler et al., 2004). The binding site of SNX5 with CHC22 was mapped to a domain which is equivalent to that which comprises the interaction interface between clathrin light chains (CLC) and CHC17 (Chen et al., 2002; Wilbur et al., 2010). SNX5 and the functionally-redundant paralogue protein SNX6, encoded by a duplicated gene, comprise a membrane remodeling BAR and a Phox homology (PX) domain, with the latter serving as a cargo-binding domain instead of the canonical lipid binding associated with PX domains (Kvainickas et al., 2017; Simonetti et al., 2019). These SNX-BAR protein family members were initially implicated in Retromer sorting at endosomes by homology with yeast proteins (Rojas et al., 2007; Simonetti and Cullen, 2018; van Weering et al., 2012; Wassmer et al., 2007). However, it is now established that SNX5/6 heterodimerize with SNX1, or its functionally-redundant paralogue protein SNX2, to form the ESCPE-1 complex, which is distinct from conventional Retromer and mediates separate endosomal sorting pathways (Evans et al., 2020; Simonetti et al., 2022; Simonetti et al., 2019). The resulting SNX-BAR ESCPE-1 heterodimers interact with lipids through the PX domain of SNX1/2 and with cargo through the PX of SNX5/6 (Evans et al., 2020; Kvainickas et al., 2017; Simonetti et al., 2017; van Weering et al., 2012).

Here, we delineate the relationship between the differential membrane recruitment of CHC22 relative to CHC17, and the unique binding partners identified for CHC22. We confirm that CHC22 binds endogenously to SNX5/6 in cells and demonstrate that this interaction is exclusive of SNX5/6 participation in the ESCPE-1 complex. We show that SNX5 directly binds p115 and that this interaction is required but not sufficient for CHC22 localization to the ERGIC and for GSC formation. The CHC22-ERGIC interaction and GSC formation were found to additionally require binding of the CHC22 TD directly to p115. This binding is disrupted by mutation of a divergent patch in the CHC22 TD compared to the equivalent residues in CHC17. We thus demonstrate that the specific localization of CHC22 to early secretory membranes requires a bipartite recruitment mechanism. CHC22 is targeted to these membranes by recognition of p115 directly via the CHC22 N-terminal domain, and indirectly through SNX5/6 bridging at the C-terminal trimerization domain. The demonstration that both interactions are essential for the formation of an insulin-responsive GSC defines key molecular determinants regulating glucose clearance in humans.

Results

SNX5/6 are required for correct localization of CHC22

CHC22 functions at the ERGIC for GLUT4 transport to the GSC (Camus et al., 2020), a pathway that is distinct from CHC17 clathrin traffic and is present in both HeLa and muscle cells. In HeLa, which endogenously express CHC22 at levels comparable to myoblasts (Esk et al., 2010), CHC22 localizes to a perinuclear region overlapping strongly with p115 and partially with GM130 (Fig. 1A) (Camus et al., 2020). To identify determinants of the perinuclear recruitment of CHC22, a quantitative image analysis methodology was developed. In brief, DAPI staining of nuclei was used to identify each cell as well as provide a signal for quantification of the perinuclear area. The area between the nuclear boundary and a dilated boundary extending a further 4.5µm created a region in which perinuclear mean fluorescence intensity (PeriMI) was measured (Fig. 1A). In wild-type unmodified HeLa cells, the cell-by-cell PeriMI of CHC22 was highly correlated with the PeriMI of p115 ($r = 0.88$, Fig. 1B) and partially correlated with the PeriMI of GM130 ($r = 0.55$, Fig. 1B′), corroborating previous observations (Camus et al., 2020) and verifying this method as a measurement of correct CHC22 localization.

To assess the effect on CHC22 distribution when SNX5 levels were altered, a HeLa cell line engineered by CRISPR to delete the genes encoding SNX5 and SNX6 *(ΔSNX5/6)*, was used (Figure 1C). This SNX5/6-null cell line was previously produced for, and characterized in, studies of Retromer and ESCPE-1 trafficking (Simonetti et al., 2022; Simonetti et al., 2017; Simonetti et al., 2019). In those studies, phenotypes were only observed when both SNX5 and SNX6 were deleted, indicating their functional redundancy. Compared to the parental HeLa line from which they were derived (Control), CHC22 distribution in *ΔSNX5/6* cells exhibited reduced perinuclear enrichment, maintaining only a diffuse pattern of staining throughout the cytoplasm (Fig. 1C). Quantification of the PeriMI of CHC22 and of CHC22 colocalization with p115 revealed a significant reduction of perinuclear enrichment ($p < 0.0001$, Fig. 1D) and p115 colocalization ($p = 0.027$, Fig. 1E) in the *ΔSNX5/6* cells. Loss of CHC22 membrane association was then confirmed by fractionation of the *ΔSNX5/6* cells and measuring ratios of membrane-associated vs cytosolic (M:C ratio) CHC22 by quantitative immunoblotting (Fig. 1F-G). Consistent with previous reports, in all cells it was possible to observe a higher proportion of CHC17 in the cytosolic fraction and a greater proportion of CHC22 on membranes (Liu et al., 2001). The relative amount of CHC22 in the membrane fraction decreased in *ΔSNX5/6* cells compared to parental control cells ($p = 0.0047$, Fig. 1G). In contrast, the CHC17 ratio between membrane-associated and cytosolic fractions was indistinguishable between the control and null cell lines.

An active role for SNX5 in CHC22 membrane recruitment was then investigated to rule out indirect effects of SNX5/6 loss. When control HeLa cells were transfected to over-express a FLAG-tagged SNX5 recombinant protein (Towler et al., 2004) (Fig. 1H), the PeriMI of CHC22 increased by a magnitude of approximately three-fold over mock-transfected control cells ($p < 0.0001$, Fig. 1I). Additionally, the ability of FLAG-tagged SNX5 to rescue the *ΔSNX5/6* cell phenotype was tested. Transfection of the *ΔSNX5/6* cells with FLAG-tagged SNX5 restored perinuclear localization of CHC22 (Fig. 1J), while mock-transfected *ΔSNX5/6* cells lacked perinuclear CHC22 (Fig. 1J). Quantification showed increased CHC22 PeriMI in the rescued cells relative to control ($p < 0.0001$, Fig. 1K), supporting a role for SNX5 in perinuclear recruitment of CHC22 and demonstrating that SNX5 alone can compensate for the loss of both SNX5 and SNX6. Together, these data indicate that CHC22 perinuclear recruitment positively correlates with the levels of SNX5/6 present in cells.

SNX5/6 binding to CHC22 is distinct from its interaction with ESCPE-1 and Retromer

The requirement of SNX5/6 for CHC22 localization raises the question of whether known partners of SNX5/6 are also involved. To address this, CHC22 localization was tested in HeLa cells lacking SNX1/2, which dimerize with SNX5/6 in the endosomal ESCPE-1 complex (Simonetti et al., 2022; Simonetti et al., 2017; Simonetti et al., 2019), with further examination of whether CHC22 localization is affected in cells lacking the human VPS26A/B:VPS35:VPS29 Retromer complex. The retromer-null (*ΔVPS35*) and SNX1/2-null cells (*ΔSNX1/2*) were produced by CRISPR engineering and characterized in earlier studies (Simonetti et al., 2022; Simonetti et al., 2017; Simonetti et al., 2019). In the *ΔVPS35* cells, neither CHC22 ($p = 0.237$, Fig. 2A-B) nor p115 ($p = 0.998$, Fig. 2A-C) perinuclear intensities were altered relative to the control, while a decrease was observed in the PeriMI of GM130 ($p < 0.0001$, Fig. 2D). By contrast, in *ΔSNX5/6* cells (Fig. 2A-E), CHC22 perinuclear mean intensity was reduced ($p < 0.0001$, Fig. 2B), as already observed (Fig. 1C-E) and the mean intensity of p115 was also reduced ($p = 0.004$, Fig. 2C), with no change detected in GM130 relative to control ($p = 0.691$, Fig. 2D). A decrease in the CHC22 total protein level in *ΔSNX5/6* cells was observed (Fig. 2E). However, as the magnitude of the reduction in total protein was less than the reduction in the PeriMI, it was inferred that changes in total levels alone did not account for the reduced amount of perinuclear CHC22 in *ΔSNX5/6* cells, suggesting loss of recruitment. Together, these data suggest that the Retromer pathway is distinct from the CHC22-SNX5/6 pathway.

By comparison, in the *ΔSNX1/2* cells, an increase was observed in CHC22 perinuclear mean intensity ($p < 0.0001$, Fig. 2F-G) relative to control cells with no change detected in p115 ($p = 0.898$, Fig. 2H). Again, the PeriMI of p115 was reduced in the *ΔSNX5/6* cells in parallel with effects on the perinuclear levels of CHC22 (Fig. 2F-I). Further, an increase in the PeriMI of GM130 was measured in the *ΔSNX1/2* cells ($p < 0.0001$, Fig. 2I), which was the opposite of the *ΔVPS35* cell phenotype. This suggested that loss of Retromer- and SNX1/2-mediated traffic can indirectly affect GM130 positive compartments (Wassmer et al., 2007). Measurement of the total protein in these cells revealed an increase of total CHC22 in the *ΔSNX1/2* cells (Fig. 2J) but by a magnitude less than that observed for the changes in perinuclear localization (Fig. 2G). In these *ΔSNX1/2* cells, the SNX5/6 present would not be participating in the ESCPE-1 complex, therefore there would be more freely available to bind CHC22. This could potentially account for the increased CHC22 perinuclear localization in these cells, similar to the effect

observed following SNX5 overexpression (Fig. 1H) and for increased stability of CHC22 through enhanced membrane association. To assess whether SNX5/6 membrane association increases in the absence of SNX1/2, *ΔSNX1/2* cells were immunostained for SNX6, as no available SNX5 antibody produced discrete signal in immunofluorescence (Fig. 2K) and an increase of SNX6 perinuclear localization in the *ΔSNX1/2* cells was observed ($p = 0.038$, Fig. 2K, L). As changes to both CHC22 and p115 localization were only observed in *ΔSNX5/6* cells, and *ΔSNX1/2* cells did not phenocopy the loss of CHC22 localization but enhanced its enrichment, the CHC22-SNX5/6 interaction appears to be distinct from the ESCPE-1 dimer, as well as from Retromer. In sum, there was a positive correlation between the levels and/or availability of SNX5/6 and the enrichment of CHC22 in the perinuclear region.

Finally, to complement the analysis of compartment markers, the distribution of the classical cargo transferrin receptor (TfR) was examined (Mayle et al., 2012). The measurement of the PeriMI of TfR in these null cells revealed an elevation only in the *ΔSNX1/2* and *ΔVPS35*, but not in *ΔSNX5/6* cells (Fig. S1). An enrichment of perinuclear TfR indicated a loss of endosomal recycling to the cell surface, consistent with previous reports of TfR distribution when Retromer components are depleted (Chen et al., 2013; Tabuchi et al., 2010). This finding further supports the functional distinction between SNX5/6 and Retromer (Simonetti et al., 2017; Simonetti et al., 2019), and is indicative of potential functional segregation of SNX5/6 and SNX1/2, as seen for CHC22 localization. Overall, these data indicate that the CHC22-SNX5/6 interaction is distinct from both the Retromer pathway and the ESCPE-1 complex.

The SNX5 BAR domain binds CHC22 at the trimerization domain (TxD)

An earlier study, following up yeast-two-hybrid evidence of CHC22-SNX5 interaction, demonstrated that FLAG-tagged SNX5 over-expressed in cells could be co-immunoprecipitated with CHC22 (Towler et al., 2004). To establish whether this interaction occurs between endogenous proteins at physiological expression levels, CHC22 was immunoprecipitated from HeLa cell lysate and from lysate of human muscle myotubes differentiated from AB1190 myoblasts (Camus et al., 2020), and the co-immunoprecipitated proteins analyzed by immunoblotting. SNX5 and SNX6 co-immunoprecipitated with CHC22 from both cell lysate preparations (Fig. 3A, B). Thus, the CHC22-SNX5/6 interaction is relevant to CHC22 function in muscle (Camus et al., 2020), as well as in HeLa cells. Further

examination of the CHC22 co-immunoprecipitates revealed that neither SNX1 nor the Retromer component VPS35 were present in complex with CHC22 (Fig. S2).

Previous yeast-two-hybrid studies mapped the CHC22-SNX5 interaction to the Hub domain of CHC22 (C-terminal third, residues 1074-1640, Fig. 3C) and to residues 238-404 of the SNX5 BAR domain and detected no interaction between SNX5 and the CHC17 Hub domain (Towler et al., 2004). To model the configuration and positioning of SNX5-CHC22 interaction, the partner protein sequences were simulated using AlphaFold multimer analysis (Jumper et al., 2021; Varadi et al., 2022) (Fig. 3C). The model was based on a shortened CHC22 Hub trimer (residues 1278-1640) plus the full BAR domain (residues 202-404) of SNX5. The configurations produced by this *de novo* interaction modeling suggested binding of the SNX5 BAR domain to the central trimerization domain (TxD, residues 1576-1640) within the Hub of CHC22 (Fig. 3D). The highest scoring model predicted that the SNX5 BAR domain binds on top of the TxD, interacting with all three heavy chain subunits within the trimer. This markedly differs from the way that clathrin light chains (CLCs) interact with the Hub region of CHC17 established by cryo-electron microscopy (Morris et al., 2019), X-ray crystallography (Wilbur et al., 2010) and mutagenesis (Chen et al., 2002). The CLCs align along the proximal leg, starting at the knee, at approximately residue 1267 (Chen et al., 2002), and interact at the sides of the helix tripod of the TxD (Morris et al., 2019), which projects to the opposite side to that predicted for SNX BAR binding. Repeating the AlphaFold simulation of the predicted interaction between CHC22 and SNX5 using the BAR domain of the SNX5 paralogue protein SNX6 (residues 216-418), generated models which were near identical to that of SNX5 (data not shown). As such, and in light of reported functional redundancy between SNX5 and SNX6, further molecular experiments focused on SNX5 alone.

The AlphaFold prediction was then tested empirically *in vitro* using recombinantly expressed protein fragments (Fig. 3E, F). First, the specificity of SNX5 for CHC22 clathrin compared to CHC17 was tested. This was achieved by showing direct binding of full-length SNX5 protein to a His-tagged Hub domain of CHC22 and not to the equivalent His-tagged CHC17 Hub (Fig. 3E) with the Hub fragments bound to Ni^{++} beads and then exposed to recombinant SNX5 protein coupled to GST (Fig. 3E). To refine the CHC22 binding site for SNX5 and investigate the prediction from AlphaFold that the TxD is involved, His-tagged CHC22 Hub or His-tagged CHC22 TxD (residues 1520-1640) were bound to beads and both were shown to capture GST-

SNX5 (Fig. 3F), demonstrating that the CHC22 TxD is sufficient to bind SNX5 and supporting the AlphaFold prediction.

Taken together, these data reveal that CHC22 is directly bound by SNX5 and that this interaction occurs at the TxD. The earlier yeast-two-hybrid data and the AlphaFold model indicate that SNX5 interaction with the TxD of CHC22 is mediated via the SNX5 BAR domain, which also mediates interaction with SNX1/2. Indeed, the binding interface of SNX5 in the ESCPE-1 complex, predicted by homology modeling (Simonetti et al., 2019) is highly overlapping with that predicted by AlphaFold for the SNX5-CHC22 interface (Fig. 3G). Overlaying the SNX1-SNX5 ESCPE-1 dimer with the predicted CHC22-SNX5 interaction interface further suggested steric hinderance between ESCPE-1 and CHC22-SNX5 interactions (Fig. 3H), indicating that these two SNX5 complexes are probably mutually exclusive. To investigate SNX5-CHC22 binding further, a series of SNX5 point mutants with known defects in binding cargo (PX domain) and in binding SNX1 (BAR domain), were assessed for binding to CHC22 TxD. The mutants tested were cargo binding mutant (F136D) (Simonetti et al., 2019), and two phosphorylation site-mutants (S226A and S226E) known to affect SNX1/2 interaction (Itai et al., 2018; Simonetti et al., 2019). Binding was detected between the CHC22 TxD and all full length SNX5 mutants, as well as full length wild-type SNX5 (Fig. 3I), indicating that the CHC22-SNX5 interaction is regulated by different residues to those which regulate the SNX5-SNX1 or SNX5-cargo interactions.

SNX5 links CHC22 to the ERGIC by binding p115

Previous work identified the ERGIC tether p115 as forming a complex with CHC22 and not with CHC17 (Camus et al., 2020). Further, analysis of the high degree of correlation between the levels of CHC22 and p115 (Fig. 1B), and the localization changes observed in *ΔSNX5/6* cells (Fig. 2H) led to the question of whether p115 is involved in SNX5/6-mediated CHC22 recruitment. Immunoprecipitation of CHC22 from control parental HeLa cells compared to *ΔSNX5/6, ΔSNX1/2,* or *ΔVPS35* cells showed that co-precipitation of p115 was lost in the *ΔSNX5/6* cells, but present in the others (Fig. 4A, B). This suggested that SNX5/6 binding contributes to the interaction between CHC22 and p115.

In previous analyses of the CHC22-p115 interaction, it was observed that p115 is a target for CHC22 localization at the ERGIC, as siRNA-mediated knockdown (KD) of CHC22 did not

affect p115, but p115 KD altered CHC22 distribution (Camus et al., 2020). To interrogate the role of SNX5/6 in CHC22 recruitment by p115, siRNA-mediated KD was used to deplete p115 (p115 KD) and assess whether SNX5 could still rescue CHC22 localization (Fig. 4C-E). In control HeLa cells, displacement of CHC22 and GM130 was observed following p115 KD compared to cells treated with control (scrambled) siRNA (Fig. 4C, second row), consistent with previous reports (Camus et al., 2020). In *ΔSNX5/6* cells, p115 KD did not further affect the displacement of CHC22 (Fig. 4C, third row). However, in p115-depleted *ΔSNX5/6* cells, CHC22 perinuclear localization could not be restored by transfection of FLAG-tagged SNX5 (Fig. 4C, bottom) as previously observed when p115 was present (Fig. 1J). Quantifying the PeriMI of both CHC22 and GM130 confirmed these observations; p115 KD resulted in a reduction of both CHC22 ($p < 0.0001$, Fig. 4D) and GM130 ($p < 0.0001$, Fig. 4E) compared to cells treated with control siRNA. No significant change was detected between the three p115 KD conditions, irrespective of expression of the FLAG-SNX5 rescue construct ($p = 0.125$-0.969, Fig. 4D, E), whereas a significant change in CHC22 localization was measured between control and each of the p115 KD conditions ($p <0.0001$ for each, Fig. 4D). This indicated that SNX5 is required for CHC22 recruitment by p115. Purified recombinant full-length SNX5 was then tested for *in vitro* binding to recombinant full-length His-p115 and found to bind p115 directly, compared to GST alone (Fig. 4F). Thus, SNX5 acts as a bridge between CHC22 and p115, explaining its role in CHC22 localization.

A unique patch in the N-terminal domain of CHC22 is also required for p115 binding

CHC17 clathrin is recruited to membranes by interactions with adaptor proteins at the N-terminal domain (TD) (Chen et al., 2020; Lemmon and Traub, 2012). This raised the question as to whether CHC22 membrane recruitment by the SNX5-p115 interaction is both necessary and sufficient for CHC22 recruitment, or whether interactions mediated by the CHC22 TD are also involved in its localization. To investigate this, a CHC22 mutant lacking the TD (residues 1-330) (ΔTD) was created and tagged with super-folded GFP (sfGFP) (Fig. 5B). This protein was expressed in HeLa cells by transfection and its localization compared to a wild-type (WT) sfGFP-tagged control (Fig. 5A). The WT sfGFP-CHC22 localized to the perinuclear region overlapping with p115 (Fig. 5A). By contrast, the ΔTD CHC22 construct had no discrete localization pattern but was present throughout the cytoplasm (Fig. 5A, bottom). Quantification of CHC22-p115 colocalization (Fig. 5C) showed WT sfGFP-CHC22 had a mean colocalization value of 0.45, similar to the value calculated for endogenous CHC22 (Fig. 1E), whereas sfGFP-

ΔTD-CHC22 had a significantly lower colocalization coefficient with p115 (mean value 0.32, $p < 0.0001$, Fig. 5C). This indicated that the CHC22 TD is also required for correct CHC22 localization in addition to the SNX5-p115 interaction.

To assess whether the CHC22 TD is involved with the p115 interaction, GFP nano-trap reagents were used to isolate GFP-tagged WT-CHC22, ΔTD-CHC22 and WT-CHC17 from lysates of HeLa cells transiently transfected to express the encoding GFP-constructs (Fig. 5D). These nano-trap isolates were probed for p115 by immunoblotting (Fig. 5D). Relative to WT CHC22, the ΔTD CHC22 showed significantly reduced binding to p115, though not as low as CHC17 (Fig. 5E). The residual CHC22-p115 binding can be attributed to interactions involving SNX5 at the C-terminus. To establish whether the CHC22 TD (residues 1-330) directly binds p115, a recombinant His-tagged CHC22 TD fragment was tested for pulldown of recombinant GST-p115 (Fig. 5F). This TD fragment bound full-length p115 and a recombinant fragment of GGA2, a preferred partner for CHC22 over CHC17 (Camus et al., 2020; Esk et al., 2010; Vassilopoulos et al., 2009). CHC22 TD did not bind the β2-subunit of AP2, consistent with previously demonstrated lack of co-immunoprecipitation of AP2 (Liu et al., 2001; Vassilopoulos et al., 2009) and the fact that CHC22 lacks a role in endocytosis (Dannhauser et al., 2017; Esk et al., 2010). By contrast, the TD of CHC17 interacted with GGA2 and AP2, and not with p115, indicating the specificity of CHC22 TD for p115 (Fig. 5G).

To better understand the molecular basis for CHC22-adaptor binding specificity, potential adaptor binding sites used by CHC22 were assessed by analyzing the sequence conservation between the TDs of CHC17 and CHC22. All of the previously mapped CHC17 residues involved in adaptor binding sites were conserved between the two TDs (Fig. 6A). This implied that either subtle structural perturbations in these binding sites alter their specificity, and/or that additional binding sites unique to CHC22 are responsible for mediating its specific localization. To search for potential unique binding sites, regions of the CHC22 TD that are divergent in sequence between CHC17 and CHC22 were identified on a homology model, derived from the CHC17 TD, and colored based on its sequence conservation relative to CHC17 (Fig. 6B). This revealed spatial clustering of nine divergent residues which is not apparent from the primary amino acid sequence alone. To investigate the effect of these differences, each of the divergent residues in CHC22 TD was mutated to the equivalent CHC17 TD residue, creating a chimeric construct CHC22-TD-Chim (Chim). To determine if these

residues dictate the specificity of the CHC22 TD-p115 interaction, *in vitro* binding was performed using WT and Chim protein and the interaction with p115 assessed. The Chim mutant did not bind p115 (Fig. 6C), supporting the notion that the divergent patch in CHC22 is responsible for some of the unique CHC22 TD interactions. Overall, these data indicate that the CHC22 TD can bind directly to p115 independently of the SNX5/6-TxD interaction at the C-terminus. Furthermore, this interaction requires a divergent patch within the CHC22 TD which is not shared by CHC17.

Bipartite recruitment of CHC22 to the ERGIC is required for formation of the insulin-responsive GLUT4 storage compartment.

Having identified two molecular interactions by which CHC22 is recruited to ERGIC membranes containing p115, the functional relevance of both interactions in CHC22-dependent membrane traffic were addressed. The most well-characterized CHC22 cargo is the insulin-responsive glucose transporter GLUT4 (Camus et al., 2020; Fumagalli et al., 2019; Gould et al., 2020; Vassilopoulos et al., 2009). To interrogate the role of both CHC22 recruitment mechanisms in GLUT4 transport, a HeLa cell line stably transfected to express a HA-GLUT4-GFP fusion construct (HeLa-G4) was used. The HA tag is located on an exofacial loop to enable detection of the GLUT4 located at the cell surface, while the C-terminal GFP tag enables measurement of the total GLUT4 population (Martin et al., 2006). Due to HeLa cells expressing CHC22, comparable to muscle tissue (Esk et al., 2010), and all the other components of the trafficking pathway, the HeLa-G4 cell line packages GLUT4 in a GSC and releases GLUT4 to the cell surface in response to insulin (Bruno et al., 2016; Camus et al., 2020; Martin et al., 2006).

The role of SNX5/6 in GLUT4 traffic was initially assessed by fluorescent recovery after photobleaching (FRAP) of the perinuclear storage compartment (Cheng et al., 2010; Eyster et al., 2006; Fumagalli et al., 2019; Greig and Bulgakova, 2021; Ishikawa-Ankerhold et al., 2012; Khalique et al., 2016; Kitamura and Kinjo, 2018) (Fig. 7A-C). In HeLa-G4 cells treated with control siRNA, the mobile fraction of HA-GLUT4-GFP in the GSC was approximately 50% (Fig. 7A-B). The recovery curve was best fit by a two-phase exponential model with the two components potentially representing diffusion and steady state membrane traffic (Pincet et al., 2016; Sprague and McNally, 2005). In HeLa-G4 cells depleted of both SNX5 and SNX6 by siRNA-mediated KD, GLUT4-GFP recovery dynamics were slowed, with the mobile fraction reduced to 40%. Nonlinear regression analysis showed a significant difference in the recovery

curves, using a sum of squares F-test to determine if the recovery curve differed between the datasets ($p < 0.0001$, Fig. 7A-B). By contrast, following siRNA treatment to deplete the Retromer component VPS35, no significant change in perinuclear GLUT4-GFP dynamics was detected ($p = 0.061$, Fig. 7C). Thus, SNX5/6 are implicated in the general mobility dynamics and steady-state trafficking of GLUT4.

To examine the role of SNX5/6 in enabling the formation of a functional insulin-responsive GSC, the insulin-stimulated surface translocation of HA-GLUT4-GFP was assessed after SNX5/6 KD (Fig. 7D, E). Translocation was determined by flow cytometry (Camus et al., 2020; Fumagalli et al., 2019) and quantified as the median fluorescent intensity (MFI) of surface GLUT4 (HA signal) relative to the total GLUT4 (GFP signal) (Fig. 7D-G). Insulin-stimulated translocation was significantly lost in cells following SNX5/6 KD or CHC22 KD ($p = 0.358$, $p = 0.683$ respectively, Fig. 7E), while in control cells, an increase of 50% was observed between the basal and insulin-stimulated surface:total GLUT4 ratio (Fig. 7E), consistent with previous reports, and typical for GLUT4 translocation in muscle cells (Camus et al., 2020; Fumagalli et al., 2019). By contrast, when either SNX5 or SNX6 were depleted alone, GLUT4-GFP translocation was still observed ($p = 0.002$ and $p = 0.012$, respectively, Fig.7E), suggesting functional redundance of SNX5 and SNX6 in this pathway. For comparison, VPS35 KD did not impair HA-GLUT4-GFP translocation in response to insulin ($p = 0.015$, Fig. 7E).

To assess the functional role of the CHC22 TD-p115 interaction in GLUT4 translocation, HeLa cells expressing HA-GLUT4-GFP were depleted of CHC22 by siRNA-mediated KD and tested for rescue of GLUT4-GFP translocation by transfection with siRNA-resistant WT CHC22 or ΔTD CHC22 (Fig. 7F, G). In these cells, transfection with WT CHC22 rescued the insulin-stimulated translocation of GLUT4-GFP ($p = 0.038$, Fig. 7G), while following transfection with the ΔTD CHC22 construct no significant change in surface GLUT4-GFP after insulin stimulation was detected ($p = 0.79$, Fig. 7G). Together, these functional assays indicate that the CHC22 TD and SNX5/6 interactions are both required to enable CHC22 activity, which is a prerequisite for the formation of the perinuclear GLUT4 storage compartment, and that neither recruitment mechanism can sustain CHC22 function without the other.

Discussion

This study has characterized the molecular mechanism by which CHC22 clathrin is specifically recruited to the early secretory pathway, where it targets GLUT4 to the GSC. We have demonstrated that CHC22 recognizes the ERGIC tether p115 via both direct binding at N-terminal domain and indirectly at the C-terminus by interacting with SNX5. Disruption of either interaction impairs CHC22 recruitment and abrogates translocation of GLUT4 in response to insulin. This bipartite recruitment of CHC22 is fundamentally distinct from the recruitment mechanism of canonical CHC17 clathrin, which provides an explanation of how CHC22 can function at a different intracellular location from CHC17.

Our findings have now contextualized earlier results showing that CHC22 participates in two separate complexes with GLUT4; one involving AP1 and GGA2 and one involving p115 and IRAP. Both of which are proposed to facilitate GLUT4 sorting to the GSC from the endosome and the ERGIC respectively (Camus et al., 2020; Gould et al., 2020; Hosaka et al., 2005). In addition to highlighting the role of p115 in the recruitment of CHC22 to the ERGIC, the present study establishes the mechanism of how SNX5/6, which was identified as a CHC22 partner in an earlier study (Towler et al., 2004), enables CHC22's distinct function at the ERGIC. Our study defines a function for SNX5, and its SNX6 paralogue, that is independent of their participation in the endosomal recycling ESCPE-1 complex.

We thus propose a model whereby CHC22 is recruited to the early secretory pathway through a bipartite mechanism mediated by interaction with p115 via both the N- and C-terminal domains of CHC22 (Fig. 8, interaction 1 and 2). The SNX5/6 interaction at the CHC22 C-terminal domain may act as the first step in a sequential interaction that then enables the CHC22 N-terminal domain to dock onto p115, in a more conventional adaptor-like interaction, typical of CHC17. This idea is supported by the fact that separate loss of these interactions each results in mis-localization of CHC22, indicating non-redundancy. As p115 contains a long tail domain approximately 45nm in length (Striegl et al., 2009), it is topologically possible that p115 can sustain two interactions with CHC22 spanning the thickness of the clathrin lattice, reaching the SNX5/6 present on the upper surface of the TxD and the TD oriented internal to the lattice. The flexible hinge region of the AP2 adaptor complex has been shown to extend over a similar range to link the clathrin lattice to the plasma membrane in CHC17-coated vesicles (Kovtun et al., 2020).

Our demonstration of a direct interaction between a SNX-BAR protein and a clathrin heavy chain raises the question of the extent to which the clathrin and ESCPE-1 pathways intersect. Prior to the present study, the best studied clathrin-interacting sorting nexin was sorting nexin 9 (SNX9), which was identified as an interactor of CHC17 at the plasma membrane to facilitate endocytosis by remodeling actin and enabling scission of vesicles (Soulet et al., 2005). Furthermore, it was demonstrated that CHC17 was not involved in the formation of SNX-dependent carriers (McGough and Cullen, 2013). By contrast, in this study we show the CHC22 clathrin isoform binds SNX5 through its C-terminal domain and requires only SNX5/6 and not the full ESCPE-1 complex to associate with ERGIC membranes. Our work suggests that CHC22 does not use SNX-BAR for its capacity to induce membrane curvature, as the BAR domain directly binds to the CHC22 TxD (Fig. 3). Rather, the SNX interaction appears to be used for p115 binding to mediate interactions which specify CHC22 localization. In this capacity, SNX5/6 seem to be acting independently of SNX1/2 as depletion of the latter did not reduce CHC22 localization with p115 and SNX1 is not present in CHC22 immunoprecipitates (Fig. S2). Depletion of SNX1/2 increased CHC22 perinuclear recruitment, as observed for over-expression of SNX5, suggesting that the levels of SNX5/6 available to bind and recruit CHC22 were increased by SNX1/2 depletion (Fig. 2). Overall, these findings indicate that CHC22 clathrin is repurposing a SNX-BAR protein to facilitate recognition of ERGIC membranes, which is an unconventional organelle for clathrin recruitment.

Prior evidence for any SNX protein involvement in the early secretory pathway is limited, although some recent data has indicated that the SNX-BAR family member SNX19 tethers and positions endoplasmic reticulum exit sites (Saric et al., 2021). Other recent findings suggest a role for SNX-BAR proteins in the formation of autophagosomes and in xenophagy, both originating from ER/ERGIC membranes (Dong et al., 2021; Nemec et al., 2017; Wu et al., 2022). Our study further expands this emerging view of SNX activity beyond the endosomal system, in which they were first described, by showing interaction with the ERGIC tether protein p115. We demonstrate that this binding is an innate property of SNX5 (Fig. 4) suggesting the possibility that SNX-BAR proteins could be involved in early secretory membrane traffic in other species.

It has been reported that assembly and disassembly of the ESCPE-1 complex is influenced by phosphorylation of SNX5/6 at the interface with SNX1/2 (Itai et al., 2018). Interestingly, mutation of SNX5 to a phosphomimetic residue that abrogates SNX1/2 binding had no effect

on SNX5 binding to CHC22 (Fig. 3I). Although the AlphaFold prediction suggests the CHC22-SNX5 interaction uses the same interface as predicted for SNX5 to bind SNX1/2, the CHC22-SNX5 interface appears to be dependent on different residues. Notably, mutation of the cargo-binding motif in the SNX5 PX domain did not affect p115 interaction, further suggesting that the SNX5 role in CHC22 recruitment involves different SNX5 properties than those regulating its function in the ESCPE-1 complex, as well as being independent of the activity of that complex.

The TxD of CHC22 alone is sufficient to bind SNX5, in a manner distinct from the configuration of the clathrin light chains (CLC) interaction with the hub (C-terminal third) region of CHC17. Our AlphaFold modeling predicts that the CHC22-SNX5 interaction could extend 40 angstroms along the proximal leg of the CHC22 triskelion. By comparison, the CLC interaction with CHC17 extends from the side of the TxD along the triskelion leg to its characteristic bended knee (125 angstroms from the TxD) (Wilbur et al., 2010). CHC22 immunoprecipitated from cells and the purified CHC22 Hub do not bind CLCs, and anti-CLC antibodies do not co-localize with CHC22 in cells, although CHC22-CLC interactions can be detected by yeast-two-hybrid assays (Dannhauser et al., 2017; Liu et al., 2001; Towler et al., 2004). The original mapping of SNX5 binding to the CHC22 Hub domain by yeast-two-hybrid suggested that SNX5 might be a CLC substitute for CHC22 (Towler et al., 2004). In so far as SNX5 interacts with the TxD, it may provide the trimer-stabilizing function imparted by CLC to CHC17 (Ybe et al., 2007). Indeed, recent phylogenetic studies identifying CLCs of highly divergent sequences in protist eukaryotes (Santos et al., 2022) indicate that CLC equivalents are predicted to interact with the TxD of CHC17 equivalents, and that this may be the essential molecular requirement for a CHC-associated subunit. As SNX5/6 interacts principally with the TxD of CHC22 rather spanning the proximal leg of the heavy chain to the knee where CLC affects CHC17 assembly dynamics (Redlingshöfer and Brodsky, 2021), one possibility is that SNX5/6 binding influences the CHC22 uncoating dynamics. CHC22 has markedly different uncoating properties to CHC17 (Dannhauser et al., 2017) and the truncation of the TxD in CHC22 relative to CHC17, losing the recognition site for the uncoating ATPase (Rapoport et al., 2008), is the most striking distinction between the two clathrin isoforms (Liu et al., 2001).

This study further revealed the first direct evidence of the TD of CHC22 mediating adaptor interactions *in vivo*. This is consistent with the clathrin recruitment paradigm derived from CHC17, in which the TD comprises four separate binding sites that interact with a collection

of well-studied adaptor proteins to recruit clathrin to distinct cellular compartments (Briant et al., 2020; Chen et al., 2020; Lemmon and Traub, 2012; Smith et al., 2017; Wood and Smith, 2021). As both CHC22 and CHC17 share some interactors (e.g., GGA2, AP1), but are distinct in others (e.g., AP2 and AP3) (Dannhauser et al., 2017; Esk et al., 2010; Liu et al., 2001), it was predicted that some divergence within the TD accounted for CHC22 recruitment specificity. However, all the known adaptor binding sites in CHC17 are conserved in CHC22. When the CHC22 TD was modeled on the known structure of CHC17 TD, a divergent patch of nine residues on the surface of the CHC22 TD was identified (Fig. 6). Notably, when the residues comprising this patch were all mutated to the equivalent CHC17 residues, p115 binding was abolished. This observation suggests that the identified patch influences CHC22 TD conformation to regulate adaptor specificity, enabling a role for the TD in differential recruitment of CHC22 relative to CHC17.

Overall, a bipartite mechanism for the recruitment of the specialized CHC22 clathrin isoform to the early secretory pathway, a localization distinct from canonical CHC17, was identified and characterized. Using the insulin-responsive glucose uptake transporter GLUT4 as an exemplar, we found that this dual interaction is functionally required to form a mature GSC from which GLUT4 can translocate to the cell surface upon insulin stimulation. Several cargoes, including CFTR, αps1-integrin, and several types of nutrient transporters are known to bypass the Golgi from the early secretory pathway, as observed for the CHC22-mediated GLUT4 pathway (Camus et al., 2020; Dimou et al., 2022; Grieve and Rabouille, 2011; Schotman et al., 2008; Tveit et al., 2009). As such, the CHC22 recruitment mechanism defined in this study could be a broader feature of early secretory trafficking.

Materials and Methods

Cell culture

All cell lines were cultured at 37ºC in a 5% CO_2 atmosphere with 100% humidity. HeLa cells were grown in DMEM high glucose (Gibco) supplemented with 10% FBS (Gibco), 50 U/ml penicillin, 50 µg/ml streptomycin (Gibco). The HeLa lines used in this study were as follows: Parental (Control for the null cell lines), SNX1/2 Null (*ΔSNX1/2*), SNX5/6 Null (*ΔSNX5/6*), VPS35 Null (*ΔVPS35*) (Simonetti et al., 2019), and HA-GLUT4-GFP (Camus et al., 2020). The human myoblast cell line AB1190 was grown in complete Skeletal Muscle Cell Growth Medium (Promocell) with provided supplemental cocktail and 10% FBS (Gibco) to reach a

15% final supplement concentration (volume/volume) (Camus et al., 2020). Differentiation of the AB1190 myoblasts was induced when culture was near fully confluent (>90%) by changing to Skeletal Muscle Cell Differentiation Medium (Promocell) and culturing for a further 12-14 days: with provided insulin supplement only. All cell lines used tested negative for mycoplasma infection.

siRNA

Targeting and nontargeting siRNA was synthesized (Qiagen or Thermo Fisher Scientific) to interact with mRNA against the following sequences: CHC22 (5′-TCGGGCAAATGTGCC AAGCAA-3′ and 5′-AACTGGGAGGATCTAGTTAAA-3′,1:1 mixture of siRNAs were used) (Camus et al., 2020), p115 (5′-AAGACCGGCAATTGTAGTACT-3′) (Camus et al., 2020), SNX5 (5′-UUAGUUUCAGCCCGAAGCAUC-3'), SNX6 (5′-UUAUGAGGUAGACGACUAAAU-3') (Wassmer et al., 2007), VPS35 (ID 132357, AM16708) (Predesigned – Thermo Fisher Scientific).

Plasmid constructs

The FLAG-SNX5 construct was used for rescue and SNX5 overexpression experiments (Towler et al., 2004). For the terminal domain (TD) experiments, sfGFP-CHC22 and GFP-CHC17-encoding plasmids were used (Esk et al., 2010) either in full-length or as a template for creation of deletion mutants and chimeras. In brief, the plasmid encoding the full-length protein was used as a template to design primers to amplify all but the region desired to be deleted. These were generated and transformed into DH5α competent E. coli cells using Q5 mutagenesis kit in accordance with the manufacturer's instructions (NEB). For rescue FACS with WT-CHC22 or ΔTD-CHC22, the sfGFP-WT-CHC22 and sfGFP-ΔTD-CHC22 plasmids were used as a template for exchanging the fluorescent tag from sfGFP to mApple (mApple encoding donor plasmid was a gift from Dr Samantha J. Warrington, Lab of Prof David Strutt, University of Sheffield) a HiFi (NEB) reaction was used to exchange the sfGFP for mApple using overlapping primers, in accordance with the manufacturer's instructions.

Transfection

HeLa cells were seeded at a density of 15,000 cell/cm^2 in either 24-well plates or 12-well plate on #1.5 glass coverslips (Thermo Fisher Scientific). The following day, cells were observed to ensure satisfactory attachment and confluency (50-70%) before proceeding. For transfection

of siRNA, oligonucleotides were complexed with jetPRIME (Polyplus) in accordance with manufacturer's instructions and added to the cells to a final concentration of 20 nM for all targets. Cells were then returned to normal growth conditions and harvested for analysis or fixed for microscopy imaging 72 h later. Depletion was confirmed by immunoblotting. For transfection of DNA plasmids, cells were seeded at the same density and the following day, were transfected with plasmid DNA which was complexed with jetPRIME in a 1:2 mixture (DNA/jetPRIME) in accordance with manufacturer's instructions. For SNX5 and CHC22 plasmids 0.5 µg of DNA was used per well in a 12-well dish. Cells were then returned to normal growth conditions and harvested for analysis or fixed for microscopy imaging 24 h later. For FACS experiments requiring both siRNA and DNA plasmid transfection, a combination of the two protocols were used: cells were seeded, transfected the following day with siRNA and 48 h later transfected again with plasmid DNA. Cells were harvested for analysis or fixed for microscopy imaging the following day at the 72 h post-initiation endpoint.

Antibodies

The primary antibodies used in this study were used at a dilution of 1:200-1:500 for IF, for immunoblotting the primary antibodies were used at a dilution of 1:2000-1:5000. The primary antibodies used in this study include: mouse monoclonal α-p115 (clone 7D1) (Waters et al., 1992), rabbit polyclonal α-CHC22 (22283-1-AP, Proteintech), goat polyclonal α-SNX5 (ab5983, abcam), rabbit polyclonal α-SNX5 (ab180520, abcam), rabbit polyclonal α-SNX6 (ab247087, abcam), goat polyclonal α-VPS35 (ab10099, abcam), goat polyclonal α-GM130 (sc-16268, Santa Cruz), rabbit polyclonal α-TfR (ab84036, abcam), mouse monoclonal α-tubulin (ab7291, abcam), mouse monoclonal α-HA (16B12, BioLegend), mouse monoclonal α-FLAG (M2 no.1804. Sigma), mouse monoclonal α-His, (MAB050H, R&D Systems), rabbit polyclonal α-GST, (#2622, Cell Signaling).

Secondary antibodies were used as follows: For IF, species-specific secondaries conjugated to, Alexa Fluor 488, Alexa Fluor 555, or Alexa Fluor 647 (Thermo Fisher Scientific) were used at a dilution of 1:1000. For quantitative western immunoblotting, secondaries conjugated to IRDye were used, α-mouse 680RD and α-rabbit 800CW (LI-COR Biosciences) at a dilution of 1:10,000. For SNX5 and SNX6 fluorescent immunoblotting the primary antibodies were directly conjugated with DyLight 800 dye using conjugation kit, in accordance with manufacturer's instructions (DyLight™, Thermo Fisher Scientific). For western blotting,

antibodies coupled to horseradish peroxidase (HRP, Bio-Rad) were used at a dilution of 1:5000.

Immunofluorescent staining

Cells were seeded on #1.5 glass coverslips (Thermo Fisher Scientific) in dishes and experimental procedures (transfection, insulin stimulation etc.) performed. At the endpoint of experiments, cells were washed once with PBS, then fixed in 4% PFA for 20 min at room temperature (21°C). After this, the cells were washed three times with PBS. The cells were then permeabilized in PBST (PBS with 0.2% Triton X-100) for 10 min, the cells were then blocked in PBST with 2% horse serum (Gibco) for 1 hour at room temperature. For staining, the cells were incubated with primary antibody solution (diluted in PBST) overnight at 4°C. The following day the cells were washed three times in PBS and incubated with secondary antibodies (diluted in PBST) for 1-2 h at room temperature. Cells were then washed once in PBS before the addition of a DAPI staining solution to mark the nuclei (DAPI at 1:10,000 in PBS) for 20 min. After this time, the cells were washed a further three times before the coverslips were mounted on microscope slides (Superfrost, Thermo Fisher Scientific) using 2ul of Vectashield (Vector Laboratories) and sealed with nail varnish.

Image acquisition and analysis

All samples were imaged using a Leica TCS SP8 inverted laser-scanning confocal microscope equipped with two high-sensitivity hybrid detectors and one photomultiplier. A 63x (1.40 NA) HC Plan-Apo CS2 oil-immersion objective was used with five laser lines. Fluorophores were sequentially excited at 405 nm (DAPI), 488 nm (GFP, Alexa Fluor 488), 543 nm (Alexa Fluor 555), 561 nm (Alexa Fluor 568), and 633 nm (Alexa Fluor 647). For fixed images, 8-bit images were acquired (1024x1024 XY pixel aspect) without further digital magnification. For each image, a Z-axis sectional stack was acquired using the nuclear DAPI signal as a positional marker. This consisted of 9 sections with a 0.5 µm intersectional spacing, corresponding to a total Z-axis length of 4 µm. The images were saved in the Leica binary image format (.lif) and exported for further processing. For analysis, the images were processed using a series of custom macros in Fiji (NIH). In brief, the images were sorted by number and channel and, for each individual channel, an average intensity projection of the Z-section was extracted, created, and sorted. For analysis of the perinuclear mean intensity (PeriMI), the DAPI channel was used to create two masks for each cell in each image: one of the original dimensions of the nucleus, the other dilated by a factor corresponding to an isotropic increase in radius of 4.5 µm. The

two masks were applied to the average intensity projection of the channels to be quantified using a macro incorporating the 'Analyze particles' function in Fiji. This measured the area and total pixel values for the original and dilated areas for each channel, which was saved as a .csv file. These data were then processed using a custom script in R. In brief, for each channel, the area and total pixel intensity of the original dimension mask images (corresponding to a background for all perinuclear and cytoplasmic proteins) was subtracted from the dilated mask values. The corrected total pixel values were then divided by the corrected area to generate the mean intensity value for each cell in each image. These perinuclear mean intensity values were exported as .csv for subsequent statistical analysis. For colocalization, the images were processed in the same manner and analysis performed using the JACoP plugin (Bolte and Cordelieres, 2006) in Fiji, generating Pearson's correlation coefficients, the application of which is indicated in the text and figure legends.

Live imaging and FRAP

All live imaging and FRAP experiments were performed using the HeLa HA-GLUT4-GFP cell line. Cells were seeded on 35 mm glass bottom dishes (VWR) at standard density, 3-4 days prior to imaging. The day after seeding, the cells were transfected as previously described. On the day of imaging, cells were changed to a serum-free media compatible with live imaging: FluoroBrite DMEM (Gibco) for 2 h prior to imaging. This mitigated the effects of insulin contained in serum and enabled measurement of the basal dynamics of the storage compartment. The cells were imaged using the Leica TCS SP8 confocal microscope previously described, with the following environmental modifications: the incubation chamber around stage was adjusted to a temperature of 37°C with a 5% CO_2 atmosphere. For the FRAP experiments, 8-bit images were taken at a magnification of 0.28 µm pixel−1 (512 x 512 pixels XY-image). In each cell, a single circular region of interest (ROI) of 7.08 µm diameter was used to encompass the area containing the HA-GLUT4-GFP in the perinuclear storage compartment. Photobleaching was performed with 1 scan at 675 nsec pixel^{-1} using 70% 488 nm laser power resulting in reduction of GLUT4-GFP signal by 70–80%. Images were taken using continuous acquisition at a frame rate of 2 s^{-1}. Prior to bleaching, a sequence of five images was taken, and a total of 100 frames corresponding to 70 sec were taken. For each dish, a total of 10-12 cells were photobleached per condition.

GLUT4 translocation assay using flow cytometry

All translocation experiments used the HeLa HA-GLUT4-GFP cell line. Cells were seeded in 6-well plates at standard density and, the following day, transfected with siRNA for KD and incubated for 72 h thereafter. For the TD rescue experiments the cells were re-transfected with expression plasmids in fresh media at the 48 h post KD time point and processed 24 h later, at the 72 h endpoint for all FACS experiments. On the day of the experiment, cells were washed (three times, PBS, 37°C) and serum starved in EBSS (Gibco) for 2 h prior to insulin stimulation. For insulin stimulation, insulin (Sigma) or the same volume of vehicle (water) was added to the wells, to a final concentration of 170 µM, for 20 min at 37°C. The cells were then placed on ice and washed with PBS containing magnesium and calcium ions ($PBS^{+/+}$) (Corning) which had been pre-cooled to 4°C, for a total of three times. The cells were then live stained by blocking for 30 min ($PBS^{+/+}$ + 2% horse serum) on ice and then incubating with anti-HA antibody solution (1:200 diluted in $PBS^{+/+}$+ 2% horse serum) on ice for 1 h to detect surface GLUT4. After this, cells were washed three times in $PBS^{+/+}$ and fixed in 4% PFA for 15 min on ice. After fixation, cells were washed three times in PBS at room temperature. After this, cells were incubated with secondary antibody solution (anti-Mouse Alexa Fluor 647 diluted 1:1000 in PBS+ 2% horse serum) for 1 hour at room temperature. Cells were then washed three times in PBS and gently lifted using a cell scraper (Corning). These suspensions were pelleted by centrifugation at 300x g for 3 min and resuspended in a 500 µL of PBS. Flow cytometry data was acquired with FACS Diva acquisition software on a LSRII flow cytometer (Becton Dickinson) equipped with violet (405 nm), blue (488 nm), yellow (561), and red (633 nm) lasers. Typically, 10,000 events were acquired, and median fluorescent intensity (MFI) values for surface GLUT4 (Alexa Fluor 647), CHC22 transfectants (mApple), and total GLUT4 (GFP) were recorded. Post-acquisition analysis was performed using FlowJo software (TreeStar), where debris was removed by using forward/side light scatter gating. Then fluorescence histograms were analyzed, using gating to select only the transfected cell populations in the TD rescue experiments based on the fluorescent signal (mApple) from the expression of the fusion protein. The MFI values were exported and processed in Excel (Microsoft), whereby the ratios of surface-to-total MFI were calculated to quantify the extent of GLUT4 translocation in each condition.

Protein extraction and immunoblotting

Protein extracts from cells were quantified by BCA (Pierce), separated by SDS-PAGE (10% acrylamide, Merck Millipore), transferred to nitrocellulose membrane (0.2 µm, Bio-Rad), labelled with primary antibodies (1–5 µg/ml), washed, and labelled with species-specific HRP-

conjugated secondary antibodies (Thermo Fisher Scientific). HRP activity was detected using Western Lightning Chemiluminescence Reagent (GE Healthcare). The molecular migration position of transferred proteins was compared with the PageRuler Prestain Protein Ladder 10–180 kDa (Themo Fisher Scientific). Signal quantification was performed using Fiji.
For quantitative western blotting, samples were prepared and processed in the same manner as standard immunoblotting. However, species-specific IRDye-conjugated secondary antibodies were added at a dilution of 1:10,000 (LI-COR Biosciences). These labelled membranes were imaged using the Odyssey DLx imaging system (LI-COR Biosciences). Quantification of the relative abundance of proteins in the membranes was performed using Image Studio (LI-COR Biosciences).

Immunoprecipitation

Cells from 10 cm^2,15 cm^2, or 500 cm^2 dishes were scraped on ice, washed in PBS precooled to 4°C and pelleted at 300x g, for 3 min, at 4°C. The pellets were resuspended in cold lysis buffer (20 mM HEPES pH 7.5, 150 mM NaCl, 1 mM EDTA, 1 mM EGTA, 10% vol/vol Glycero1, and 0.25% vol/vol Triton X-100) supplemented with protease and phosphatase inhibitors (2 mM Na_3VO_4, 1 tab/10 ml; Thermo Fisher Scientific). Cell suspensions were lysed using mechanical shearing by pipetting and then sonicated (10-15 pulses at 50% power). These lysates were centrifuged (16,000x g for 15 min, 4°C) to remove nuclei and cellular debris. The protein content of these lysates was quantified using BCA (Pierce). 1 µg of specific α-CHC22 antibody (Proteintech) was incubated with 1 ml of 5-10 mg/ml of precleared post-nuclear lysates overnight at 4°C. The samples were then incubated with washed and pre-blocked protein G Sepharose beads (50 µl, GE Healthcare) for 45 mins at 4°C, before three consecutive washing steps in lysis buffer. The pelleted protein G Sepharose beads were then resuspended in 50 µl of 2x Laemmli sample buffer (Bio-Rad) and proceeded to SDS-PAGE and immunoblotting analysis.

Membrane fractionation

Cells from 10 cm^2 or 15 cm^2 plates were scraped on ice, washed in PBS precooled to 4°C and pelleted at 300 g, for 3 min, at 4°C. The pellets were resuspended in fractionation buffer (20 mM HEPES pH 7.5, 400 mM Sucrose, 1 mM EDTA, 1 mM PMSF, 1 mM Na_3VO_4) supplemented with protease inhibitors (1 tab/10 ml; Thermo Fisher Scientific). Cells were mechanically sheared by 20x passages through a 20G needle (BD Microlance). These lysates

were centrifuged (1,000x g for 10 min, 4°C) to remove nuclei. The supernatant was then centrifuged (100,000x g for 1 h, 4°C) to separate the cytosolic fraction from the membrane fraction. After this, the supernatant (cytosolic fraction) was removed and both the resulting pellet (Membranes fraction) and a corresponding sample of the cytoplasmic fraction were denatured in either 1x (Membrane fraction) or 4x (Cytoplasmic fraction) Laemmli sample buffer before proceeding to SDS-PAGE and immunoblotting analysis.

Protein expression and purification (bacterial)

CHC22 Hub (1074-1640) and CHC22 TxD (1521-1640) were cloned into vector backbones derived from pET-Duet and pET15b, respectively, to encode N-terminal 6xHis fusions. Plasmid pIY119 encoding an N-terminal 6xHis p115 fusion was a gift from Igor Yakunin (Munro lab, LMB, Cambridge). CHC22 Hub was expressed into Rosetta 2 pLysS *E. coli* and induced with 0.4 mM IPTG at 18°C for 18 h. CHC22 TxD+ was expressed in BL21(DE3) and induced with 0.5 mM IPTG at 30°C for 5 h. p115 was expressed in BL21(DE3) and induced with 0.4 mM IPTG at 18°C for 18 h. AP2-hinge-appendage (591-937), GGA2-hinge-GAE (316-613) and p115 (1-962) were cloned into pGEX-derived vector backbones as N-terminal GST-fusions and were induced in BL21(DE3) with 0.4 mM IPTG at 18°C for 18 h.

CHC22 TD (1-364) and CHC17 TD (1-364) were cloned as N-terminal His-bdSUMO fusions and induced in Rosetta 2 pLysS *E. coli* at 37°C for 4 h with 0.5 mM IPTG. Cell pellets were lysed in TD lysis buffer (50 mM Tris pH 8, 300 mM NaCl, 5% glycerol, 25 mM imidazole) and the lysate was clarified at 40,000x g. TD+ proteins were purified using Ni affinity chromatography (HisTrap, Cytiva) and size exclusion chromatography (HiLoad 16/30 Superdex 75). Full-length SNX5 (1-404), was cloned into pGEX3 vector backbones to encode N-terminal GST-fusions. Expression plasmids were transformed into Rosetta 2 pLysS *E. coli* and induced with 0.4 mM IPTG at 18°C for 18 h. For protein purification, cell pellets were lysed by sonication in GST lysis buffer (20 mM Tris pH 8, 400 mM NaCl, 10% glycerol, 2 mM EDTA, 1 mM beta-mercaptoethanol, 1% Triton X-100, 1 mM PMSF, EDTA-free protease inhibitor) and the lysate clarified by centrifugation at 40,000x g. Fusion proteins were subsequently purified by GST affinity chromatography (GSTrap HP, Cytiva) and size exclusion chromatography (Superdex 200 HR 10/300, Cytiva).

In vitro binding assay/ protein pulldowns

For pulldowns with GST-SNX5, His-CHC22-hub, His-TxD+, His-p115 were affinity purified onto Ni-NTA HisPur beads from crude *E. coli* lysate in His purification buffer (50 mM Tris pH 8, 500 mM NaCl, 10 mM imidazole, 5% glycerol, 1 mM PMSF, EDTA-free protease inhibitor (Roche). For each pulldown 20 µL of beads were pre-blocked in His PD buffer (50 mM Tris pH 8, 300 mM NaCl, 2 mM EDTA, 1 mM BME, 2% BSA) and incubated with 15 µg of purified GST-only or GST-SNX5, in 250 µL His PD buffer for 45 mins. Pulldowns were analyzed by western blot analysis using antibodies directed against His, GST, SNX5 and p115. For pulldowns with His-TD+, GST adaptor fusions were affinity-purified onto glutathione beads (Gluthathione Sepharose High Performance, Cytiva) from crude *E. coli* lysate in GST adaptor buffer (20 mM HEPES pH 7.5, 150 mM NaCl, 2 mM BME, 1 mM EDTA, 1 mM PMSF EDTA-free protease inhibitor (Roche). For each pulldown, 20 µL of glutathione beads were pre-blocked in CHC22 PD buffer (20 mM HEPES pH 7.5, 300 mM NaCl, 0.05% NP-40, 1 mM EDTA, 50 mM NaSCN, 2 mM BME, 2% BSA) and incubated with 12.5 µg His-SUMO-CHC22TD+ or His-SUMO-CHC17TD+ for 45 mins. Pulldowns were analyzed by immunoblotting using antibodies directed against His and GST.

Homology modeling (CHC22 TD)

A homology model of the CHC22 TD (1-330) was generated using SWISS-MODEL using a previously solved crystal structure of the CHC17 TD as a template (ter Haar et al., 1998) (PDB: 1BP0).

AlphaFold modeling

A model of a single SNX5 BAR domain (202-404) complexed with a shortened CHC22-Hub (1278-1640) trimer (encoded by three individual chains) was generated using AlphaFold 2-multimer (Version 1.2.0)

GFP nano-trap precipitations

GFP immunoprecipitations were carried out using GFP-Trap agarose beads (ChromoTek) according to the manufacturer's instructions, with the addition of 10% glycerol into GFP IP lysis and GFP IP dilution buffers. For each GFP immunoprecipitation, a 10 cm dish was seeded with control HeLa cells at higher density of 2 million cells/dish and allowed to attach for 24 h. The following day, cells were transfected with 5 µg plasmid using JetPRIME (Polyplus) according to the manufacturer's instructions. After 18 h, cells were scraped and incubated on ice with gentle agitation for 30 mins in 200 µL GFP IP lysis buffer (10 mM Tris pH 7.5, 150

mM NaCl, 0.5 mM EDTA, 0.5% NP-40, 10% glycerol, EDTA-free protease inhibitor, 1 mM PMSF and 4 mM Na_3VO_4). The lysate was cleared by centrifugation at 17,000x g for 10 mins and was added to 300 µL GFP IP dilution buffer (10 mM Tris, 150 mM NaCl, 0.5 mM EDTA, 10% glycerol, EDTA-free protease inhibitor, 1 mM PMSF and 4 mM Na_3VO_4). Diluted lysates were incubated with 20 µL GFP-Trap agarose beads with end-over-end rotation for 1 h at 4°C. Beads were washed three times and the IPs analyzed by Western blot analysis.

Statistical analysis

Statistical analysis was performed in GraphPad Prism (https://www.graphpad.com/scientific-software/prism/). First, the data were cleaned using ROUT detection of outliers in Prism, followed by testing for normal distribution (D'Agostino - Pearson normality test). Then, the significance for parametric data was tested by either one-way ANOVA followed by Tukey's or Dunnett's post-hoc multiple comparison test, or an unpaired two-tailed *t*-test with Welch's correction. Detailed statistical information for each experiment, including statistical test, number of independent experiments, p values, and definition of error bars are listed in individual figure legends. For GLUT4-GFP FRAP, the bleached ROI, control ROI and background intensity were measured using the 'Time Series Analyzer' plugin in Fiji (NIH) for each time point. These data were then processed in Excel. First, the intensity of the bleached ROI at each time point was background-subtracted and normalized as follows: $I_n=(F_n-BG_n)/(FC_n-BG_n)$, where: F_n is intensity of the bleached ROI at the time point n; FC_n, intensity of the control unbleached ROI of the same size at the plasma membrane at the time point n; and BG_n, background intensity, measured with the same size ROI in cytoplasm at the time point n. Then the relative recovery at each time point was calculated using the following formula: $R_n=(I_n-I_1)/(I_0-I_1)$, where I_n, I_1 and I_0 are normalized intensities of bleached ROI at time point n, immediately after photobleaching, and before photobleaching, respectively. These values were input to Prism and nonlinear regression analysis was performed to test for best-fit model and if recoveries were significantly different between cell borders or genotypes. The recovery was fitted to either a single exponential model of the form $f(t)=1-F_{im}-A_1e^{-t/T_{fast}}$, or a bi-exponential model of the form $f(t)=1-F_{im}-A_1e^{-t/T_{fast}}-A_2e^{-t/T_{slow}}$, where F_{im} is the size of the immobile fraction, T_{fast} and T_{slow} are the half-times, and A_1 and A_2 are amplitudes of the fast and slow components of the recovery, respectively. An *F*-test was used to choose the model and compare datasets (Greig

and Bulgakova, 2021). Details about graphical representations and error bars are listed in the corresponding figure legends.

Summary of supplementary material

Fig. S1 Investigation of Transferrin receptor (TfR) distribution and localization in SNX null HeLa cell lines. Fig. S2 CHC22 immunoprecipitation from control HeLa cells with immunoblotting for VPS35 and SNX1.

Acknowledgments

The authors would like to acknowledge the contributions of Dr Stéphane M. Camus, erstwhile postdoctoral fellow of the Brodsky lab, who helped at the initiation of the work presented in this study, and Dr Manuel Giménez-Andrés, of the Cullen lab, for arranging the generous gifts of plasmids and reagents. Furthermore, the authors would like to acknowledge the contributions of non-author lab members who provided critique of the data at lab meetings and helped proof-read and edit this manuscript: particularly the contributions of Dr Will P. Bultitude, Dr Kit Briant, and Dr Lauren Foltz.

The cell culture studies reported here use the HeLa cell line. The authors would like to acknowledge Henrietta Lacks, and the HeLa cell line that was established from her tumor cells, which have made significant contributions to scientific progress and advances in human health.

This work was supported by grants to F.M. Brodsky from the Wellcome Trust (107858/Z/15/Z) and UKRI Medical Research Council (MR/S008144/1). G.T. Bates was supported by a Wellcome Trust 4-year interdisciplinary PhD studentship (219856/Z/19/Z). P.J. Cullen is supported by the Wellcome Trust (104568/Z/14/Z and 220260/Z/20/Z), the MRC (MR/L007363/1 and MR/P018807/1), the Lister Institute of Preventive Medicine, and the award of a Royal Society Noreen Murray Research Professorship (RSRP/R1/211004).

Author Contributions

J.G: conceptualization, investigation, formal analysis, supervision, software, writing–original draft, review, and editing. G.T.B: conceptualization, investigation, formal analysis, supervision, review, and editing. D.I.Y: investigation, formal analysis. B.S: conceptualization, review, and editing. P.J.C: conceptualization, supervision, review, and editing. F.M.B:

conceptualization, supervision, formal analysis, funding acquisition, project administration, writing–original draft, review, and editing.

Conflicts of Interest

The authors declare no competing financial interests.

References

Bogan, J.S. 2012. Regulation of glucose transporter translocation in health and diabetes. *Annu Rev Biochem*. 81:507-532.

Bolte, S., and F.P. Cordelieres. 2006. A guided tour into subcellular colocalization analysis in light microscopy. *J Microsc*. 224:213-232.

Briant, K., L. Redlingshofer, and F.M. Brodsky. 2020. Clathrin's life beyond 40: Connecting biochemistry with physiology and disease. *Curr Opin Cell Biol*. 65:141-149.

Bruno, J., A. Brumfield, N. Chaudhary, D. Iaea, and T.E. McGraw. 2016. SEC16A is a RAB10 effector required for insulin-stimulated GLUT4 trafficking in adipocytes. *J Cell Biol*. 214:61-76.

Camus, S.M., M.D. Camus, C. Figueras-Novoa, G. Boncompain, L.A. Sadacca, C. Esk, A. Bigot, G.W. Gould, D. Kioumourtzoglou, F. Perez, N.J. Bryant, S. Mukherjee, and F.M. Brodsky. 2020. CHC22 clathrin mediates traffic from early secretory compartments for human GLUT4 pathway biogenesis. *J Cell Biol*. 219:e201812135.

Chen, C., D. Garcia-Santos, Y. Ishikawa, A. Seguin, L. Li, K.H. Fegan, G.J. Hildick-Smith, D.I. Shah, J.D. Cooney, W. Chen, M.J. King, Y.Y. Yien, I.J. Schultz, H. Anderson, A.J. Dalton, M.L. Freedman, P.D. Kingsley, J. Palis, S.M. Hattangadi, H.F. Lodish, D.M. Ward, J. Kaplan, T. Maeda, P. Ponka, and B.H. Paw. 2013. Snx3 regulates recycling of the transferrin receptor and iron assimilation. *Cell Metab*. 17:343-352.

Chen, C.Y., M.L. Reese, P.K. Hwang, N. Ota, D. Agard, and F.M. Brodsky. 2002. Clathrin light and heavy chain interface: alpha-helix binding superhelix loops via critical tryptophans. *EMBO J*. 21:6072-6082.

Chen, Z., R.E. Mino, M. Mettlen, P. Michaely, M. Bhave, D.K. Reed, and S.L. Schmid. 2020. Wbox2: A clathrin terminal domain-derived peptide inhibitor of clathrin-mediated endocytosis. *J Cell Biol*. 219:e201908189.

Cheng, Z.J., R.D. Singh, T.K. Wang, E.L. Holicky, C.L. Wheatley, D.A. Bernlohr, D.L. Marks, and R.E. Pagano. 2010. Stimulation of GLUT4 (glucose transporter isoform 4) storage vesicle formation by sphingolipid depletion. *Biochem J*. 427:143-150.

Dannhauser, P.N., S.M. Camus, K. Sakamoto, L.A. Sadacca, J.A. Torres, M.D. Camus, K. Briant, S. Vassilopoulos, A. Rothnie, C.J. Smith, and F.M. Brodsky. 2017. CHC22 and CHC17 clathrins have distinct biochemical properties and display differential regulation and function. *J Biol Chem*. 292:20834-20844.

Dimou, S., M. Dionysopoulou, G.M. Sagia, and G. Diallinas. 2022. Golgi-Bypass Is a Major Unconventional Route for Translocation to the Plasma Membrane of Non-Apical Membrane Cargoes in Aspergillus nidulans. *Front Cell Dev Biol*. 10:852028.

Dong, X., Y. Yang, Z. Zou, Y. Zhao, B. Ci, L. Zhong, M. Bhave, L. Wang, Y.C. Kuo, X. Zang, R. Zhong, E.R. Aguilera, R.B. Richardson, B. Simonetti, J.W. Schoggins, J.K. Pfeiffer, L. Yu, X. Zhang, Y. Xie, S.L. Schmid, G. Xiao, P.A. Gleeson, N.T. Ktistakis, P.J. Cullen, R.J. Xavier, and B. Levine. 2021. Sorting nexin 5 mediates virus-induced autophagy and immunity. *Nature*. 589:456-461.

Esk, C., C.Y. Chen, L. Johannes, and F.M. Brodsky. 2010. The clathrin heavy chain isoform CHC22 functions in a novel endosomal sorting step. *J Cell Biol*. 188:131-144.

Evans, A.J., J.L. Daly, A.N.K. Anuar, B. Simonetti, and P.J. Cullen. 2020. Acute inactivation of retromer and ESCPE-1 leads to time-resolved defects in endosomal cargo sorting. *J Cell Sci*. 133.

Eyster, C.A., Q.S. Duggins, G.J. Gorbsky, and A.L. Olson. 2006. Microtubule network is required for insulin signaling through activation of Akt/protein kinase B: evidence that insulin stimulates vesicle docking/fusion but not intracellular mobility. *J Biol Chem*. 281:39719-39727.

Fumagalli, M., S.M. Camus, Y. Diekmann, A. Burke, M.D. Camus, P.J. Norman, A. Joseph, L. Abi-Rached, A. Benazzo, R. Rasteiro, I. Mathieson, M. Topf, P. Parham, M.G. Thomas, and F.M. Brodsky. 2019. Genetic diversity of CHC22 clathrin impacts its function in glucose metabolism. *eLife*. 8:e41517.

Gould, G.W., F.M. Brodsky, and N.J. Bryant. 2020. Building GLUT4 Vesicles: CHC22 Clathrin's Human Touch. *Trends Cell Biol*. 30:705-719.

Greig, J., and N.A. Bulgakova. 2021. Fluorescence Recovery After Photobleaching to Study the Dynamics of Membrane-Bound Proteins In Vivo Using the Drosophila Embryo. *Methods Mol Biol*. 2179:145-159.

Grieve, A.G., and C. Rabouille. 2011. Golgi bypass: skirting around the heart of classical secretion. *Cold Spring Harb Perspect Biol*. 3.

Hosaka, T., C.C. Brooks, E. Presman, S.K. Kim, Z. Zhang, M. Breen, D.N. Gross, E. Sztul, and P.F. Pilch. 2005. p115 Interacts with the GLUT4 vesicle protein, IRAP, and plays

a critical role in insulin-stimulated GLUT4 translocation. *Mol Biol Cell*. 16:2882-2890.

Hoshino, S., K. Sakamoto, S. Vassilopoulos, S.M. Camus, C.A. Griffin, C. Esk, J.A. Torres, N. Ohkoshi, A. Ishii, A. Tamaoka, B.H. Funke, R. Kucherlapati, M. Margeta, T.A. Rando, and F.M. Brodsky. 2013. The CHC22 clathrin-GLUT4 transport pathway contributes to skeletal muscle regeneration. *PLoS One*. 8:e77787.

Ishikawa-Ankerhold, H.C., R. Ankerhold, and G.P. Drummen. 2012. Advanced fluorescence microscopy techniques--FRAP, FLIP, FLAP, FRET and FLIM. *Molecules*. 17:4047-4132.

Itai, N., T. Shimazu, T. Kimura, I. Ibe, R. Yamashita, Y. Kaburagi, T. Dohi, T. Tonozuka, T. Takao, and A. Nishikawa. 2018. The phosphorylation of sorting nexin 5 at serine 226 regulates retrograde transport and macropinocytosis. *PLoS One*. 13:e0207205.

Jumper, J., R. Evans, A. Pritzel, T. Green, M. Figurnov, O. Ronneberger, K. Tunyasuvunakool, R. Bates, A. Zidek, A. Potapenko, A. Bridgland, C. Meyer, S.A.A. Kohl, A.J. Ballard, A. Cowie, B. Romera-Paredes, S. Nikolov, R. Jain, J. Adler, T. Back, S. Petersen, D. Reiman, E. Clancy, M. Zielinski, M. Steinegger, M. Pacholska, T. Berghammer, S. Bodenstein, D. Silver, O. Vinyals, A.W. Senior, K. Kavukcuoglu, P. Kohli, and D. Hassabis. 2021. Highly accurate protein structure prediction with AlphaFold. *Nature*. 596:583-589.

Khalique, A., R.D. Sarwade, P.R. Pandey, M.V. Vijayakumar, M.K. Bhat, and V. Seshadri. 2016. Prolonged exposure to insulin with insufficient glucose leads to impaired Glut4 translocation. *Biochem Biophys Res Commun*. 474:64-70.

Kitamura, A., and M. Kinjo. 2018. Determination of diffusion coefficients in live cells using fluorescence recovery after photobleaching with wide-field fluorescence microscopy. *Biophys Physicobiol*. 15:1-7.

Kovtun, O., V.K. Dickson, B.T. Kelly, D.J. Owen, and J.A.G. Briggs. 2020. Architecture of the AP2/clathrin coat on the membranes of clathrin-coated vesicles. *Science advances*. 6:eaba8381.

Kvainickas, A., A. Jimenez-Orgaz, H. Nagele, Z. Hu, J. Dengjel, and F. Steinberg. 2017. Cargo-selective SNX-BAR proteins mediate retromer trimer independent retrograde transport. *J Cell Biol*. 216:3677-3693.

Lemmon, S.K., and L.M. Traub. 2012. Getting in touch with the clathrin terminal domain. *Traffic*. 13:511-519.

Leto, D., and A.R. Saltiel. 2012. Regulation of glucose transport by insulin: traffic control of GLUT4. *Nat Rev Mol Cell Biol*. 13:383-396.

Liu, S.H., M.C. Towler, E. Chen, C.Y. Chen, W. Song, G. Apodaca, and F.M. Brodsky. 2001. A novel clathrin homolog that co-distributes with cytoskeletal components functions in the trans-Golgi network. *EMBO J*. 20:272-284.

Martin, O.J., A. Lee, and T.E. McGraw. 2006. GLUT4 distribution between the plasma membrane and the intracellular compartments is maintained by an insulin-modulated bipartite dynamic mechanism. *J Biol Chem*. 281:484-490.

Mayle, K.M., A.M. Le, and D.T. Kamei. 2012. The intracellular trafficking pathway of transferrin. *Biochim Biophys Acta*. 1820:264-281.

McGough, I.J., and P.J. Cullen. 2013. Clathrin is not required for SNX-BAR-retromer-mediated carrier formation. *J Cell Sci*. 126:45-52.

Morris, K.L., J.R. Jones, M. Halebian, S. Wu, M. Baker, J.P. Armache, A. Avila Ibarra, R.B. Sessions, A.D. Cameron, Y. Cheng, and C.J. Smith. 2019. Cryo-EM of multiple cage architectures reveals a universal mode of clathrin self-assembly. *Nature structural & molecular biology*. 26:890-898.

Nemec, A.A., L.A. Howell, A.K. Peterson, M.A. Murray, and R.J. Tomko, Jr. 2017. Autophagic clearance of proteasomes in yeast requires the conserved sorting nexin Snx4. *J Biol Chem*. 292:21466-21480.

Pincet, F., V. Adrien, R. Yang, J. Delacotte, J.E. Rothman, W. Urbach, and D. Tareste. 2016. FRAP to Characterize Molecular Diffusion and Interaction in Various Membrane Environments. *PLoS One*. 11:e0158457.

Rapoport, I., W. Boll, A. Yu, T. Bocking, and T. Kirchhausen. 2008. A motif in the clathrin heavy chain required for the Hsc70/auxilin uncoating reaction. *Mol Biol Cell*. 19:405-413.

Redlingshöfer, L., and F.M. Brodsky. 2021. Antagonistic regulation controls clathrin-mediated endocytosis: AP2 adaptor facilitation vs restraint from clathrin light chains. *Cells Dev*:203714.

Rojas, R., S. Kametaka, C.R. Haft, and J.S. Bonifacino. 2007. Interchangeable but essential functions of SNX1 and SNX2 in the association of retromer with endosomes and the trafficking of mannose 6-phosphate receptors. *Mol Cell Biol*. 27:1112-1124.

Santos, R., A. Astvaldsson, S.V. Pipaliya, J.P. Zumthor, J.B. Dacks, S. Svard, A.B. Hehl, and C. Faso. 2022. Combined nanometric and phylogenetic analysis of unique endocytic

compartments in Giardia lamblia sheds light on the evolution of endocytosis in Metamonada. *BMC Biol*. 20:206.

Saric, A., S.A. Freeman, C.D. Williamson, M. Jarnik, C.M. Guardia, M.S. Fernandopulle, D.C. Gershlick, and J.S. Bonifacino. 2021. SNX19 restricts endolysosome motility through contacts with the endoplasmic reticulum. *Nat Commun*. 12:4552.

Schotman, H., L. Karhinen, and C. Rabouille. 2008. dGRASP-mediated noncanonical integrin secretion is required for Drosophila epithelial remodeling. *Dev Cell*. 14:171-182.

Simonetti, B., and P.J. Cullen. 2018. Endosomal Sorting: Architecture of the Retromer Coat. *Curr Biol*. 28:R1350-R1352.

Simonetti, B., J.L. Daly, L. Simon-Gracia, K. Klein, S. Weeratunga, C. Anton-Plagaro, A. Tobi, L. Hodgson, P.A. Lewis, K.J. Heesom, D.K. Shoemark, A.D. Davidson, B.M. Collins, T. Teesalu, Y. Yamauchi, and P.J. Cullen. 2022. ESCPE-1 mediates retrograde endosomal sorting of the SARS-CoV-2 host factor Neuropilin-1. *Proc Natl Acad Sci U S A*. 119:e2201980119.

Simonetti, B., C.M. Danson, K.J. Heesom, and P.J. Cullen. 2017. Sequence-dependent cargo recognition by SNX-BARs mediates retromer-independent transport of CI-MPR. *J Cell Biol*. 216:3695-3712.

Simonetti, B., B. Paul, K. Chaudhari, S. Weeratunga, F. Steinberg, M. Gorla, K.J. Heesom, G.J. Bashaw, B.M. Collins, and P.J. Cullen. 2019. Molecular identification of a BAR domain-containing coat complex for endosomal recycling of transmembrane proteins. *Nat Cell Biol*. 21:1219-1233.

Smith, S.M., M. Baker, M. Halebian, and C.J. Smith. 2017. Weak Molecular Interactions in Clathrin-Mediated Endocytosis. *Front Mol Biosci*. 4:72.

Soulet, F., D. Yarar, M. Leonard, and S.L. Schmid. 2005. SNX9 regulates dynamin assembly and is required for efficient clathrin-mediated endocytosis. *Mol Biol Cell*. 16:2058-2067.

Sprague, B.L., and J.G. McNally. 2005. FRAP analysis of binding: proper and fitting. *Trends Cell Biol*. 15:84-91.

Striegl, H., Y. Roske, D. Kummel, and U. Heinemann. 2009. Unusual armadillo fold in the human general vesicular transport factor p115. *PLoS One*. 4:e4656.

Tabuchi, M., I. Yanatori, Y. Kawai, and F. Kishi. 2010. Retromer-mediated direct sorting is required for proper endosomal recycling of the mammalian iron transporter DMT1. *J Cell Sci*. 123:756-766.

ter Haar, E., A. Musacchio, S.C. Harrison, and T. Kirchhausen. 1998. Atomic structure of clathrin: a beta propeller terminal domain joins an alpha zigzag linker. *Cell*. 95:563-573.

Towler, M.C., P.A. Gleeson, S. Hoshino, P. Rahkila, V. Manalo, N. Ohkoshi, C. Ordahl, R.G. Parton, and F.M. Brodsky. 2004. Clathrin isoform CHC22, a component of neuromuscular and myotendinous junctions, binds sorting nexin 5 and has increased expression during myogenesis and muscle regeneration. *Mol Biol Cell*. 15:3181-3195.

Tveit, H., L.K. Akslen, G.L. Fagereng, M.A. Tranulis, and K. Prydz. 2009. A secretory Golgi bypass route to the apical surface domain of epithelial MDCK cells. *Traffic*. 10:1685-1695.

van Weering, J.R., P. Verkade, and P.J. Cullen. 2012. SNX-BAR-mediated endosome tubulation is co-ordinated with endosome maturation. *Traffic*. 13:94-107.

Varadi, M., S. Anyango, M. Deshpande, S. Nair, C. Natassia, G. Yordanova, D. Yuan, O. Stroe, G. Wood, A. Laydon, A. Zidek, T. Green, K. Tunyasuvunakool, S. Petersen, J. Jumper, E. Clancy, R. Green, A. Vora, M. Lutfi, M. Figurnov, A. Cowie, N. Hobbs, P. Kohli, G. Kleywegt, E. Birney, D. Hassabis, and S. Velankar. 2022. AlphaFold Protein Structure Database: massively expanding the structural coverage of protein-sequence space with high-accuracy models. *Nucleic Acids Res*. 50:D439-D444.

Vassilopoulos, S., C. Esk, S. Hoshino, B.H. Funke, C.Y. Chen, A.M. Plocik, W.E. Wright, R. Kucherlapati, and F.M. Brodsky. 2009. A role for the CHC22 clathrin heavy-chain isoform in human glucose metabolism. *Science*. 324:1192-1196.

Wassmer, T., N. Attar, M.V. Bujny, J. Oakley, C.J. Traer, and P.J. Cullen. 2007. A loss-of-function screen reveals SNX5 and SNX6 as potential components of the mammalian retromer. *J Cell Sci*. 120:45-54.

Waters, M.G., D.O. Clary, and J.E. Rothman. 1992. A novel 115-kD peripheral membrane protein is required for intercisternal transport in the Golgi stack. *J Cell Biol*. 118:1015-1026.

Wilbur, J.D., P.K. Hwang, J.A. Ybe, M. Lane, B.D. Sellers, M.P. Jacobson, R.J. Fletterick, and F.M. Brodsky. 2010. Conformation switching of clathrin light chain regulates clathrin lattice assembly. *Dev Cell*. 18:841-848.

Wood, K.M., and C.J. Smith. 2021. Clathrin: the molecular shape shifter. *Biochem J*. 478:3099-3123.

Wu, Z., C. Zhou, H. Que, Y. Wang, and Y. Rong. 2022. The fate of autophagosomal membrane components. *Autophagy*:1-2.

Ybe, J.A., S. Perez-Miller, Q. Niu, D.A. Coates, M.W. Drazer, and M.E. Clegg. 2007. Light chain C-terminal region reinforces the stability of clathrin heavy chain trimers. *Traffic*. 8:1101-1110.

Figure 1. The levels of SNX5/6 correlate with the localization of CHC22 to perinuclear membranes. (**A**) Representative images of control HeLa cell immunostained for CHC22 (red in merged), p115 (green in merged), and GM130 (magenta in merged) with single channels in black and white. Merged image overlap shows all channels (right). Arrow indicates the compartment overlap in the perinuclear region. Two concentric white circles mark the boundary of the perinuclear area measured using the perinuclear mean intensity (PeriMI) method. (**B-B'**) Quantification of the cell-by-cell correlation of the PeriMI of CHC22 and p115 (**B**), and CHC22 and GM130 (**B'**). Graph shows pooled data from normalized intensity values for each channel and experiment individually with line of best fit and the corresponding r value, (n = 3, 15-22 cells per experiment). (**C**) Representative images of HeLa cells; control parental line (top), CRISPR-mediated SNX5/6 null (*ΔSNX5/6*) derived line (bottom) immunostained for CHC22 (green in merged) and p115 (magenta in merged). (**D**) PeriMI quantification of CHC22 between the HeLa lines shown in (C). Each dot represents a normalized single cell value with the mean indicated by a black line in each dataset. Statistical analysis was performed using a two-tailed Student's *t*-test with Welch's correction (n = 4, 10-20 cells per genotype per experiment). (**E**) Quantification of colocalization between CHC22 and p115 using Pearson's correlation coefficient, each dot represents the mean of all cell values for each experiment (cell number 10-20 per experiment) with the mean value for each genotype indicated by a black line. (**F**) Representative immunoblots for the membrane fractionation of lysate from control HeLa (left) and *ΔSNX5/6* HeLa (right) immunoblotted for: CHC22, CHC17, transferrin receptor (TfR), HSC70, and tubulin. Lanes show the input, cytosolic fraction, and membrane fraction respectively. The migration positions of molecular weight (MW) markers are indicated at the left in kilodaltons (kDa). (**G**) Quantification of the ratio between the membrane and cytosolic fractions (M:C) of both CHC17 and CHC22 between the control and *ΔSNX5/6* (Null) cells. Graph shows mean ± SEM. Statistical analysis was performed using a two-tailed Student's *t*-test with Welch's correction (n = 4). (**H**) Representative images of control HeLa cells either mock transfected (top) or transfected with a FLAG-SNX5 overexpression plasmid (SNX5 OE) (middle and bottom). Two rows are shown to demonstrate the range of transfection effects. Cells were immunostained for CHC22 (green in merged) and FLAG (magenta in merged) with single channels shown in black and white. (**I**) Quantification of the CHC22 PeriMI between mock (Con) and FLAG-SNX5 (OE) transfected cells in control HeLa. Each dot represents a normalized single cell value with the mean indicated by a black line in each dataset. Statistical analysis was performed using a two-tailed Student's *t*-test with Welch's correction (n = 3, 14-

25 cells per genotype, per experiment). (**J**) Representative images of mock transfected control HeLa (top), mock transfected *ΔSNX5/6* HeLa (middle), and *ΔSNX5/6* HeLa transfected with FLAG-SNX5 overexpression (OE) plasmid (*ΔSNX5/6* + SNX5 OE) (bottom). Cells were immunostained for CHC22 (green in merged) and FLAG (not shown in merged, for clarity) with single channels shown in black and white. (**K**) Quantification of the CHC22 PeriMI between control mock transfected, *ΔSNX5/6* cells mock transfected, and *ΔSNX5/6* cells transfected with FLAG-SNX5 plasmid shown in (J). Each dot represents a normalized single cell value with the mean indicated by a black line in each dataset. Statistical analysis was performed using a one-way ANOVA with a Tukey post-hoc test. (n = 3, 8-17 cells per condition, per experiment). ns = not significant; *p<0.05; **p<0.01; ****p<0.0001. Scale bars: 25 µm.

Figure 2. SNX5/6 interaction with CHC22 is independent of both VPS35 retromer and the ESCPE-1 complex. (**A**) Representative images of HeLa cells; control parental line (top), VPS35 null (*ΔVPS35*) derived line (middle), and *ΔSNX5/6* derived line (bottom) immunostained for CHC22 (red in merged), p115 (magenta in merged) and GM130 (green in merged). (**B-D**) Quantification of the PeriMI of: CHC22 (**B**), p115 (**C**), and GM130 (**D**), between control, *ΔVPS35*, and *ΔSNX5/6* HeLa cells. Each dot represents a normalized single cell value with the mean indicated by a black line in each dataset. Statistical analysis was performed using a one-way ANOVA with Dunnett post-hoc test (n = 3, 18-29 cells per genotype, per experiment). (**E**) Representative immunoblots of lysates from the three HeLa genotypes: control (con), *ΔVPS35* (VPS35) and *ΔSNX5/6* (SNX5/6) immunoblotted for: CHC22, GM130, p115, and tubulin. Normalized mean optical density (OD) values for CHC22 are shown (n = 3). The migration position of MW markers is indicated at the left in kDa. (**F**) Representative images of HeLa cells; control parental line (top), *ΔSNX1/2* derived line (middle), and *ΔSNX5/6* derived line (bottom) immunostained for CHC22 (red in merged), p115 (magenta in merged) and GM130 (green in merged). (**G-I**) Quantification of the PeriMI of: CHC22 (**G**), p115 (**H**), and GM130 (**I**), between control, *ΔSNX1/2*, and *ΔSNX5/6* HeLa cells. Each dot represents a normalized single cell value with the mean indicated by a black line in each dataset. Statistical analysis was performed using a one-way ANOVA with Dunnett post-hoc test (n = 3, 15-26 cells per genotype, per experiment). (**J**) Representative immunoblots of lysates from the three HeLa genotypes: control (con), *ΔSNX1/2* (SNX1/2) and *ΔSNX5/6* (SNX5/6) immunoblotted for: CHC22, GM130, p115, and tubulin. Normalized mean OD

values for CHC22 are shown (n = 3). The migration positions of MW markers are indicated at the left in kDa. (**K**) Representative images of HeLa cells; control parental line (top), *ΔSNX1/2* derived line (middle) and *ΔSNX5/6* derived line (bottom) immunostained for SNX6 (red in merged) and GM130 (green in merged). (**L**) Quantification of the PeriMI of SNX6 between control, SNX1/2 null, and SNX5/6 null HeLa cells. Each dot represents a normalized single cell value with the mean indicated by a black line in each dataset. Statistical analysis was performed using a one-way ANOVA with Dunnett post-hoc test (n = 3, 16-27 cells per genotype, per experiment). ns = not significant; **p<0.01; ***p<0.001; ****p<0.0001. Scale bars: 25 µm.

Figure 3. SNX5/6 bind directly to CHC22 at the trimerization domain.

(**A-B**) Representative immunoblots of immunoprecipitates of CHC22, from control HeLa (A) and differentiated human skeletal muscle (hSKMC) cell line AB1190 (B). Samples were immunoblotted for CHC22, SNX5, SNX6, and tubulin. Three lanes comprise: Input (5%), bead-only control (Bead) and CHC22 immunoprecipitate (22 IP). The migration positions of MW markers are indicated at the left in kDa (n = 4-6). (**C**) Schematic illustration of the structure of a single clathrin triskelion comprising three heavy chains, hub region of the protein is indicated by red dotted triangle. (**D**) AlphaFold prediction of the interaction between CHC22 hub and the BAR domain of SNX5. The proximal leg of CHC22 is shown in blue, the trimerization domain (TxD, residues 1520-1640) of CHC22 is shown in magenta, the SNX5 BAR domain is shown in orange. Two angles of view are displayed. (**E**) A representative immunoblot of *in vitro* binding assays between purified fragments of: CHC22 hub (His-22) or CHC17 hub (His-17), and full-length SNX5 (GST-SNX5). Samples were immunoblotted for GST, His and SNX5. Control GST-only lanes are on the left and GST-SNX5 conjugate containing lanes on the right. Four lanes in each comprise: Input (2%), bead-only control (Bead), His-tagged CHC22 hub (His-22), and His-tagged CHC17 hub (His-17). The position of MW markers is indicated at the left in kDa (n = 3-5). (**F**) Representative immunoblot of *in vitro* binding assays between purified fragments of: CHC22 hub (22 Hub) or CHC22 TxD (22 TxD), and full-length SNX5 (GST-SNX5). Samples were immunoblotted for GST, His and SNX5. Control GST-only lanes are on the left and GST-SNX5 conjugate-containing lanes on the right. Four lanes in each comprise: Input (2%), bead-only control (Bead), His-tagged CHC22 Hub (22 Hub), and His-tagged CHC22 TxD (22 TxD). The position of MW markers is indicated at the left in kDa (n = 3-5). (**G**) Schematic illustration of the SNX1-SNX5 dimer

which comprises the ESCPE-1 complex (SNX1 in cyan, SNX5 in orange). (**H**) Overlay of the ESCPE-1 dimer with the Hub region of CHC22 (Proximal legs in blue, TxD region in magenta). (**I**) Representative immunoblot of *in vitro* binding assays between purified fragments of: CHC22 TxD (22 TxD) and full-length GST-SNX5 mutants. Samples were immunoblotted for GST and His. Control GST-only lanes are on the left and GST-SNX5 conjugate-containing lanes on the right. Six lanes in each comprise: bead-only control (GST), wild-type GST-SNX5 (WT), cargo mutant GST-SNX5 (F136D), Phosphomimetic GST-SNX5 (S226A), Phosphomutant GST-SNX5 (S226E) and CHC22 TxD input (2%) (TxD) . The position of MW markers is indicated at the left in kDa (n = 2).

Figure 4. SNX5 directly binds p115, which recruits CHC22 to ERGIC membranes.
(**A**) Representative immunoblots of immunoprecipitates of CHC22, from control parental HeLa (left) and *ΔSNX5/6* derived line (right) immunoblotted for CHC22, p115, and tubulin. Three lanes comprise: Input (5%), bead-only control (Bead) and CHC22 immunoprecipitate (22 IP). The migration positions of MW markers are indicated at the left in kDa (n = 4). (**B**) Representative immunoblots of immunoprecipitates of CHC22, from *ΔSNX1/2* derived HeLa line (left) and *ΔVPS35* derived line (right) immunoblotted for CHC22, p115, and tubulin. Three lanes comprise: Input (5%), bead-only control (Bead) and CHC22 immunoprecipitate (22 IP). The migration positions of MW markers are indicated at the left in kDa (n = 4). (**C**) Representative images of HeLa cells; control parental line mock transfected (top), control parental line transfected with siRNA targeting p115 (p115 KD, second row), *ΔSNX5/6* cells transfected with siRNA targeting p115 (Null + p115 KD, third row), and *ΔSNX5/6* cells transfected with siRNA targeting p115 and FLAG-SNX5 expression plasmid (Null + p115 KD + SNX5, bottom). Cells were immunostained for CHC22 (magenta in merged), GM130 (green in merged) and FLAG (not shown in merged for clarity). (**D-E**) Quantification of the PeriMI of: CHC22 (D), and GM130 (E), between control mock transfected (Con), control transfected with p115 siRNA (p115 KD), *ΔSNX5/6* transfected with p115 siRNA (Null + p115 KD), and *ΔSNX5/6* transfected with p115 siRNA and FLAG-SNX5 expression plasmid (Null + p115 KD + SNX5) shown in (C). Each dot represents a normalized single cell value with the mean indicated by a black line in each dataset. Statistical analysis was performed using a one-way ANOVA with Dunnett and Tukey post-hoc tests (n = 3, 11-24 cells per condition, per experiment). (**F**) A representative immunoblot of *in vitro* binding assays between purified fragments of full-length p115 (His-p115) and full-length SNX5 (GST-SNX5). Samples were

immunoblotted for GST and His. Control GST-only lanes are on the left and GST-SNX5 conjugate containing lanes on the right. Three lanes in each comprise: Input (2%), bead-only control (Bead), His-tagged p115 (His-p115). The position of MW markers is indicated at the left in kDa (n = 3). ns = not significant; ****p<0.0001. Scale bars: 25 µm.

Figure 5. The N-terminal domain (TD) of CHC22 is also required for correct localization. (**A**) Representative images of HeLa cells; control parental line mock transfected (Control-top), control parental transfected with sfGFP-CHC22 wild-type expression plasmid (WT-middle), and control parental transfected with sfGFP-ΔTD-CHC22 truncated expression plasmid (ΔTD-bottom). Cells were imaged for GFP (green in merged) and immunostained for p115 (red in merged). (**B**) A schematic of the CHC22 expression plasmids, showing the location of the N-terminal sfGFP tag and the deletion of the TD in the truncated mutant (bottom). (**C**) Quantification of the Pearson's colocalization between CHC22 and p115, in cells expressing full-length sfGFP-CHC22 (WT) and sfGFP-ΔTD-CHC22 expressing cells (ΔTD). Each dot represents a single cell with the mean value for each genotype indicated by a black line (n = 3, 14-25 cells per condition, per experiment). (**D**) Representative immunoblots of GFP-tagged immunoprecipitates using anti-GFP conjugated nanotrap beads, from control HeLa cells either mock transfected (Mock), transfected with wild-type sfGFP-CHC22 plasmid (22 PD), sfGFP-ΔTD-CHC22 plasmid (ΔTD PD), or sfGFP-CHC17 plasmid (17 PD). For each condition two lanes comprise: Input (5%) and immunoprecipitate (Mock, 22 PD, ΔTD PD and 17 PD) immunoblotted for GFP and p115. The migration positions of MW markers are indicated at the left in kDa (n = 3). (**E**) A graphical representation of the intensity of the p115 signal in each condition in (D), normalized relative to the GFP signal (p115/GFP) (n = 3). (**F**) A representative immunoblot of *in vitro* binding assays between the purified TD fragment of CHC22 and the purified adaptor fragments of: AP2, GGA2, and full-length p115. Samples were immunoblotted for His. The five lanes comprise: Input of the CHC22 TD construct (His-SUMO-TD) (10%), Control beads (GST-only), the hinge appendage of AP2 (AP2 b HA), the hinge ear of GGA2 (GGA2-H-E), and full-length p115. The migration position of MW markers is indicated at the left in kDa (n = 3). (**G**) A representative immunoblot of *in vitro* binding assays between the purified TD fragment of CHC17 and the purified adaptor fragments of: AP2, GGA2, and full-length p115. Samples were immunoblotted for His. The five lanes comprise: Input of the CHC17 TD construct (His-SUMO-TD) (10%), Control beads (GST-

only), AP2 b HA, GGA2-H-E, and full-length p115. The migration position of MW markers is indicated at the left in kDa (n = 3). ****P<0.0001. Scale bars: 25 µm.

Figure 6. Divergent residues in the TD are responsible for direct CHC22 recruitment by p115.

(**A**) A graphical representation of the sequence homology analysis between the TD of human CHC22 and CHC17. Regions of identical sequence between CHC22 and CHC17 are shown in green, yellow coloring represents conservative amino acid substitutions, while red denotes radical amino acid differences between CHC22 and CHC17. (**B**) A graphical representation of the homology model analysis in (A) showing the 3-dimension configuration of the TD and the positioning of the divergent patch (red residues denoted by dashed circle). A cluster of nine residues which diverge (top) are highlighted (dashed ring), with the CHC22:CHC17 residue differences noted above. (**C**) A representative immunoblot of *in vitro* binding assays between purified CHC22 TD fragments: either wild type (WT) or chimeric (Chim), and full-length p115. Samples were immunoblotted for His. Control GST-only lanes are on the left and GST-p115 conjugate-containing lanes on the right. Two lanes in each comprise: the wild-type TD fragment of CHC22 (WT) and chimeric TD fragment (Chim). The position of MW markers is indicated at the left in kDa (n = 2).

Figure 7. Both SNX5- and TD-mediated recruitment of CHC22 are necessary for the function of the insulin-responsive GLUT4 storage compartment.

(**A-C**) Dynamics of GLUT4–GFP measured by FRAP in the HeLa HA-GLUT4-GFP (HeLa G4) stably-transfected cell line. (**A**) A representative example of FRAP in mock transfected HeLa G4 (Control), HeLa G4 transfected with siRNA targeting both SNX5 and SNX6 (SNX5/6 KD), and HeLa G4 transfected with siRNA targeting VPS35 (VPS35 KD). Panels in (A) show the position of the bleach spot (P, red circle) and the Nucleus (N, blue dashed ellipse) at the pre-bleach timepoint (T-1), bleach timepoint (T 0), and at the end timepoint (T 100). Time is in seconds. (**B**) Quantification of the HA-GLUT4-GFP fluorescence recovery post-bleaching between Control and SNX5/6 KD transfected HeLa GLUT4-GFP cells. (**C**) Quantification of the HA-GLUT4-GFP fluorescence recovery post-bleaching between Control and VPS35 KD transfected HeLa GLUT4-GFP cells. Average recovery curves (mean ± SEM) and the best-fit curves (solid lines) are shown (n = 3, 8-11 cells per experiment, per condition). (**D-E**) Insulin-stimulated GLUT4 translocation in HeLa HA-GLUT4-GFP cells measured by FACS. (**D**) Representative images of control HeLa G4 cells without (Basal) or with insulin

treatment (+Insulin). Total GLUT4 imaged using GFP tag (green in merged), surface GLUT4 detected by live immunostaining the exofacial HA tag (magenta in merged). (**E**) Quantification of the HA-GLUT4-GFP surface-to-total ratio (HA:GFP) using median fluorescent signal (MFI). HeLa GLUT4-GFP cells either mock transfected (Con) or transfected with siRNA (KD) targeting: CHC22, SNX5 and SNX6, SNX5 only, SNX6 only, or VPS35, which were then treated with vehicle only (Basal) or insulin (+Ins). Bar height represents the mean value for all experiments in each condition. Each dot represents the normalized MFI value, relative to control, for all cells in each individual experiment. Statistical analysis was performed using a two-tailed Student's *t*-test with Welch's correction between cells of the same experimental condition which were either vehicle only or insulin-treated (n = 3, 10,000 cells per condition, per experiment). (**F-G**) Insulin-stimulated GLUT4 translocation in HeLa HA-GLUT4-GFP cells measured by FACS. (**F**) Representative images of control HeLa G4 cells transfected with wild-type CHC22-mApple, without (WT Basal) or with insulin treatment (WT +Insulin) and HeLa G4 cells transfected with Terminal Domain deletion CHC22-mApple, with insulin treatment (ΔTD +Insulin). Total GLUT4 imaged using GFP tag (green in merged), CHC22-mApple constructs imaged using Apple tag (red in merged), surface GLUT4 detected by live immunostaining the exofacial HA tag (magenta in merged). (**G**) Quantification of the HA-GLUT4-GFP surface-to-total ratio (HA:GFP) using median fluorescent signal (MFI). HeLa GLUT4-GFP cells either mock transfected (Con) or transfected with siRNA (KD) targeting CHC22 alone (CHC22 KD) or combination of siRNA targeting CHC22 plus re-transfected with siRNA resistant rescue constructs: wild-type CHC22 (CHC22 WT) or siRNA targeting CHC22 plus a TD deletion rescue CHC22 (CHC22 ΔTD). These were then treated with vehicle only (Basal) or insulin (+Ins). Bar height represents the mean value for all experiments in each condition. Each dot represents the normalized MFI value, relative to control, for all cells in each individual experiment. Statistical analysis was performed using a two-tailed Student's *t*-test with Welch's correction between cells of the same experimental condition which were either vehicle only or insulin-treated (n = 4, 20,000 cells per condition, per experiment). ns = not significant; *$p<0.05$; **$p<0.01$. Scale bars: 25 µm.

Figure 8. Model of the bipartite recruitment mechanism of CHC22 to ERGIC membranes.

Schematic diagram of the proposed model for the recruitment of CHC22 by p115 to Endoplasmic reticulum-Golgi intermediate compartment membranes (ERGIC). The trimerization domain CHC22 binds SNX5, which interacts directly with p115 (interaction denoted by 1). This is complemented by the N-terminal domain of CHC22 directly binding p115 through a unique patch (Asterisk) that diverges from the CHC17 sequence (interaction denoted by 2). Disruption of either interaction abrogates CHC22 recruitment and function. The ERGIC membrane is distinguished by the localization of p115. Through the interaction of p115 with IRAP this complex is linked to the distribution and sorting of GLUT4 to an insulin-responsive intracellular compartment.

Figure S1. Transferrin receptor (TfR) distribution is altered by the loss of VPS35 and SNX1/2 but not by loss of SNX5/6

(**A**) Representative images of HeLa cells; control parental line (top), *ΔSNX1/2* derived line (second row), *ΔSNX5/6* derived line (third row), and *ΔVPS35* derived line (bottom) immunostained for TfR (magenta in merged) and p115 (green in merged). (**B**) PeriMI quantification of TfR between the HeLa lines shown in (A). Each dot represents a normalized single cell value with the mean indicated by a black line in each dataset. Statistical analysis was performed using one-way ANOVA with Dunnett post-hoc test (n = 3, 12-23 cells per genotype, per experiment). ns = not significant; *$p<0.05$; ****$p<0.0001$. Scale bars: 25 µm.

Figure S2. CHC22 is not complexed with the retromer and ESCPE-1 components VPS35 and SNX1.

(**A**) Representative immunoblots of CHC22 immunoprecipitates from control HeLa cells. Samples were immunoblotted for CHC22, VPS35, SNX1, and tubulin. Three lanes comprise: Input (5%), bead-only control (Bead) and CHC22 immunoprecipitate (22 IP). The migration positions of MW markers are indicated at the left in kDa (n = 3).

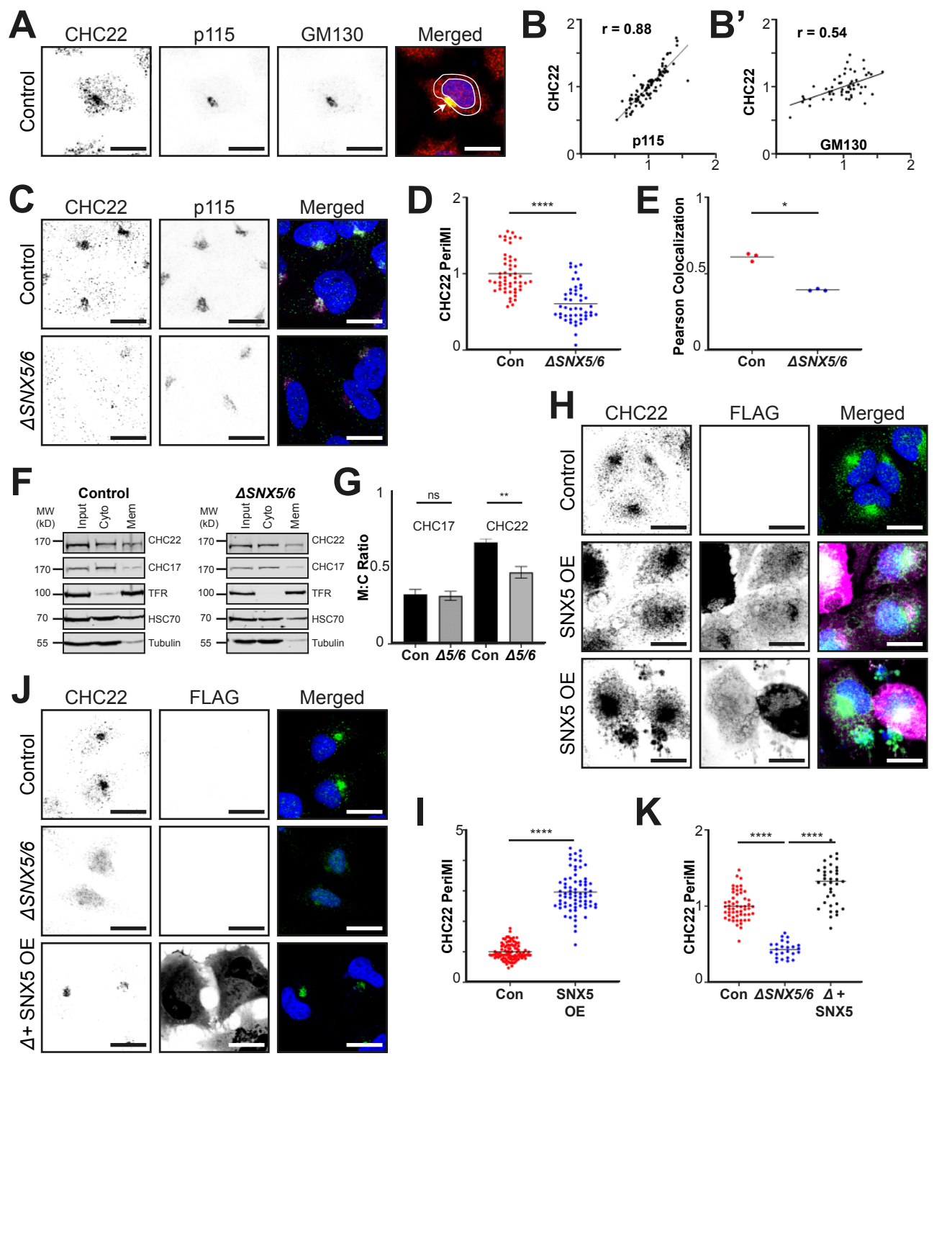
A
CHC22
p115
GM130
Merged
Control
B
r = 0.88
CHC22
p115
B'
r = 0.54
CHC22
GM130
C
CHC22
p115
Merged
Control
ΔSNX5/6
D
CHC22 PeriMI
****
Con
ΔSNX5/6
E
Pearson Colocalization
*
Con
ΔSNX5/6
F
Control
ΔSNX5/6
MW (kD)
Input
Cyto
Mem
170
CHC22
170
CHC17
100
TFR
70
HSC70
55
Tubulin
G
M:C Ratio
ns
**
CHC17
CHC22
Con
Δ5/6
Con
Δ5/6
H
CHC22
FLAG
Merged
Control
SNX5 OE
SNX5 OE
J
CHC22
FLAG
Merged
Control
ΔSNX5/6
Δ+ SNX5 OE
I
CHC22 PeriMI
****
Con
SNX5 OE
K
CHC22 PeriMI
****
****
Con
ΔSNX5/6
Δ + SNX5

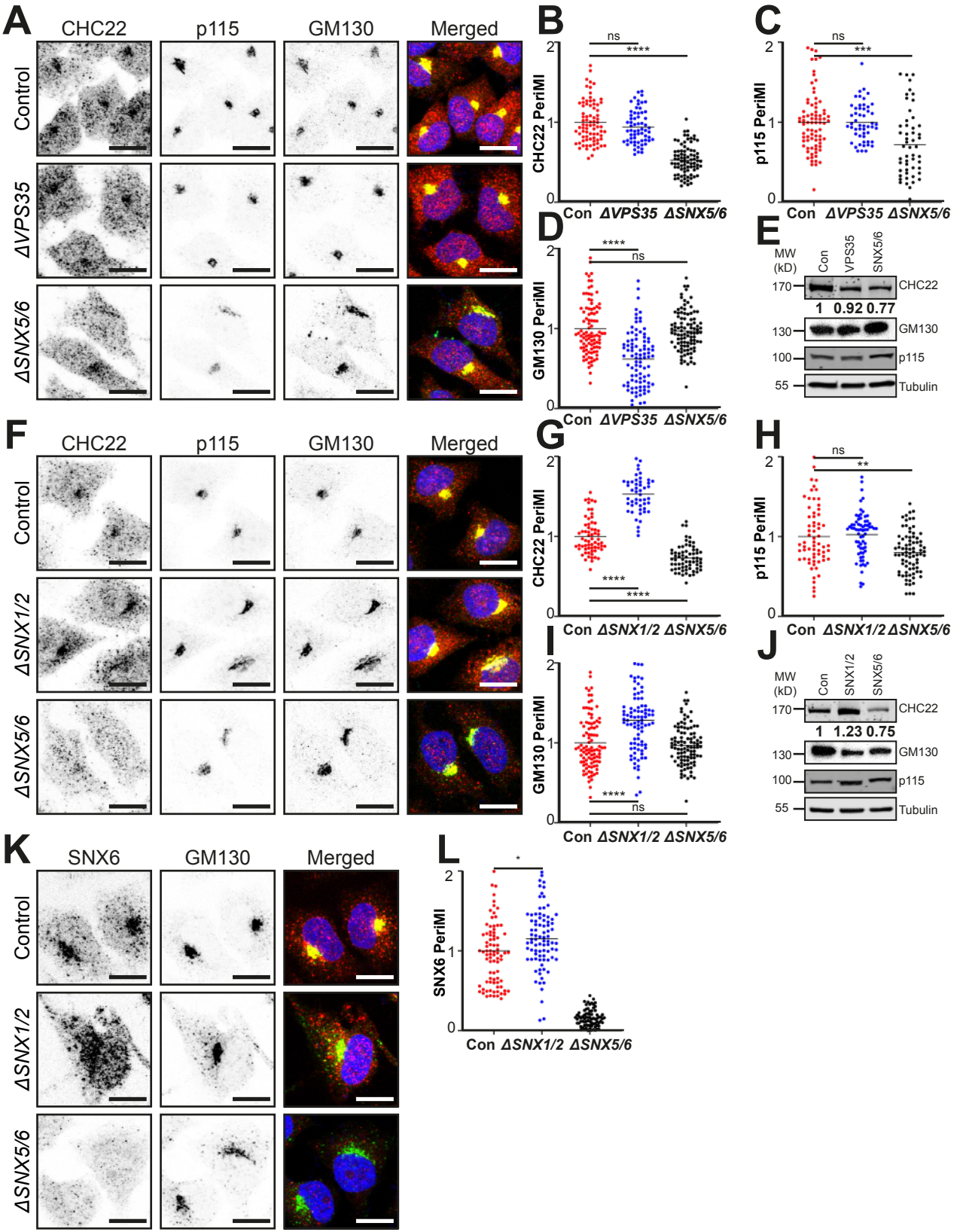
A
CHC22
p115
GM130
Merged
Control
ΔVPS35
ΔSNX5/6
B
CHC22 PeriMI
ns
****
Con
ΔVPS35
ΔSNX5/6
C
p115 PeriMI
ns
***
D
GM130 PeriMI
****
ns
E
MW (kD)
Con
VPS35
SNX5/6
170
CHC22
1 0.92 0.77
130
GM130
100
p115
55
Tubulin
F
ΔSNX1/2
G
****
H
**
I
J
SNX1/2
1 1.23 0.75
K
SNX6
L
SNX6 PeriMI
*

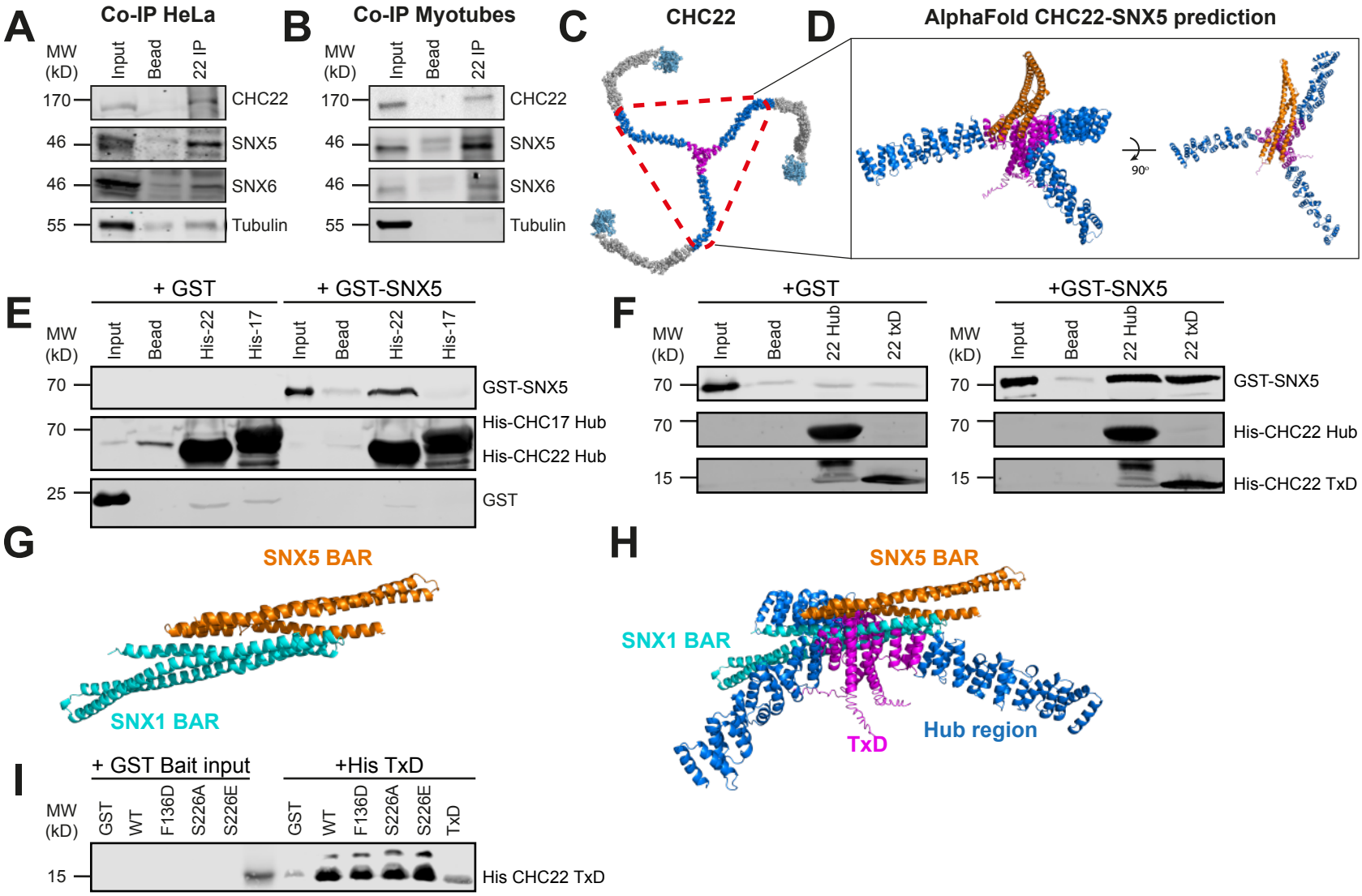
A
Co-IP HeLa
MW (kD)
Input
Bead
22 IP
170
CHC22
46
SNX5
46
SNX6
55
Tubulin
B
Co-IP Myotubes
MW (kD)
Input
Bead
22 IP
170
CHC22
46
SNX5
46
SNX6
55
Tubulin
C
CHC22
D
AlphaFold CHC22-SNX5 prediction
90°
E
+ GST
+ GST-SNX5
MW (kD)
Input
Bead
His-22
His-17
Input
Bead
His-22
His-17
70
GST-SNX5
70
His-CHC17 Hub
His-CHC22 Hub
25
GST
F
+GST
+GST-SNX5
MW (kD)
Input
Bead
22 Hub
22 txD
Input
Bead
22 Hub
22 txD
70
GST-SNX5
70
His-CHC22 Hub
15
His-CHC22 TxD
G
SNX5 BAR
SNX1 BAR
H
SNX5 BAR
SNX1 BAR
TxD
Hub region
I
+ GST Bait input
+His TxD
MW (kD)
GST
WT
F136D
S226A
S226E
GST
WT
F136D
S226A
S226E
TxD
15
His CHC22 TxD

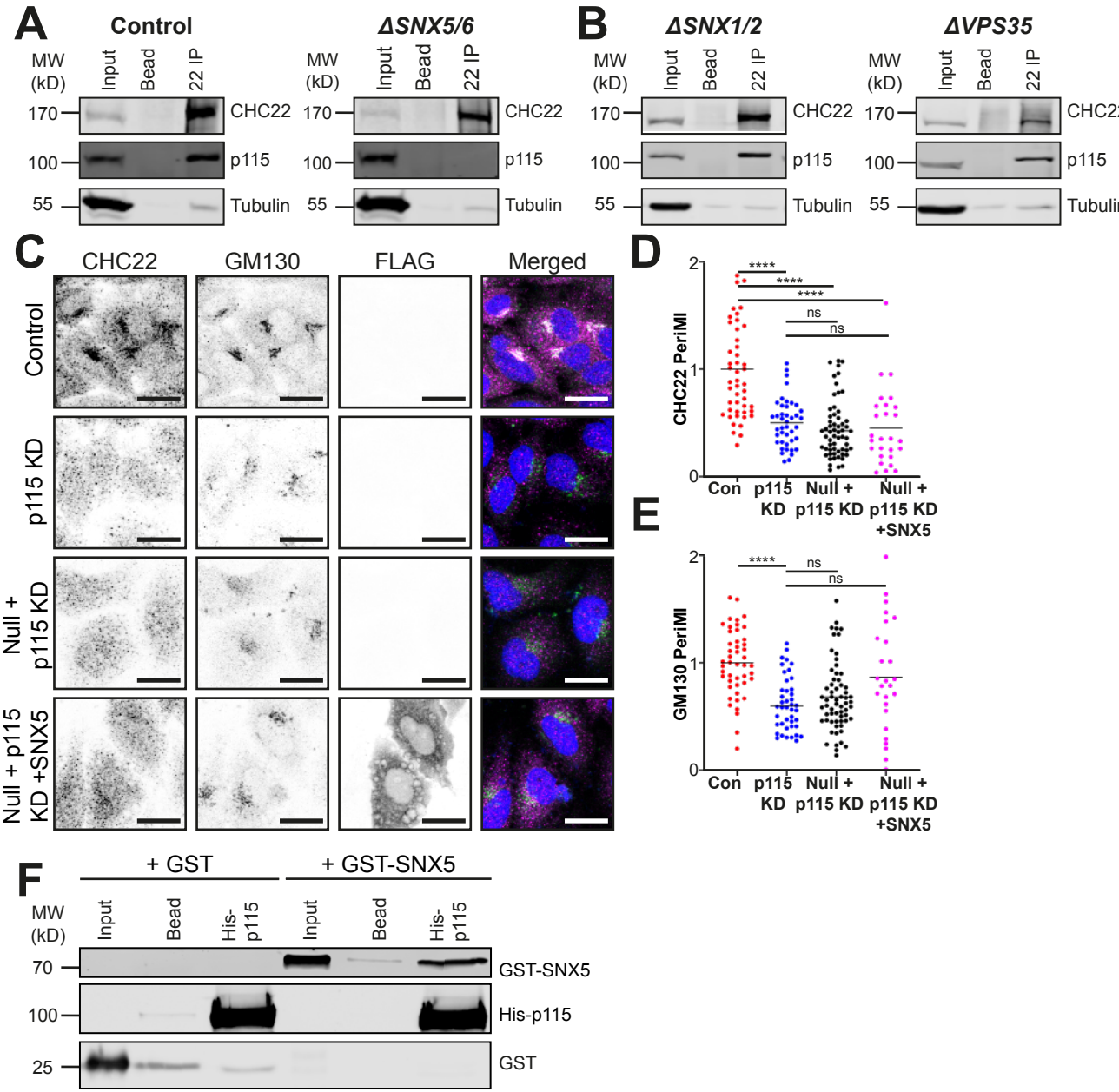
A
Control
ΔSNX5/6
MW (kD)
Input
Bead
22 IP
170
100
55
CHC22
p115
Tubulin
B
ΔSNX1/2
ΔVPS35
C
CHC22
GM130
FLAG
Merged
Control
p115 KD
Null + p115 KD
Null + p115 KD +SNX5
D
CHC22 PeriMI
****
ns
Con
p115 KD
Null + p115 KD
Null + p115 KD +SNX5
E
GM130 PeriMI
F
+ GST
+ GST-SNX5
His-p115
GST-SNX5
GST

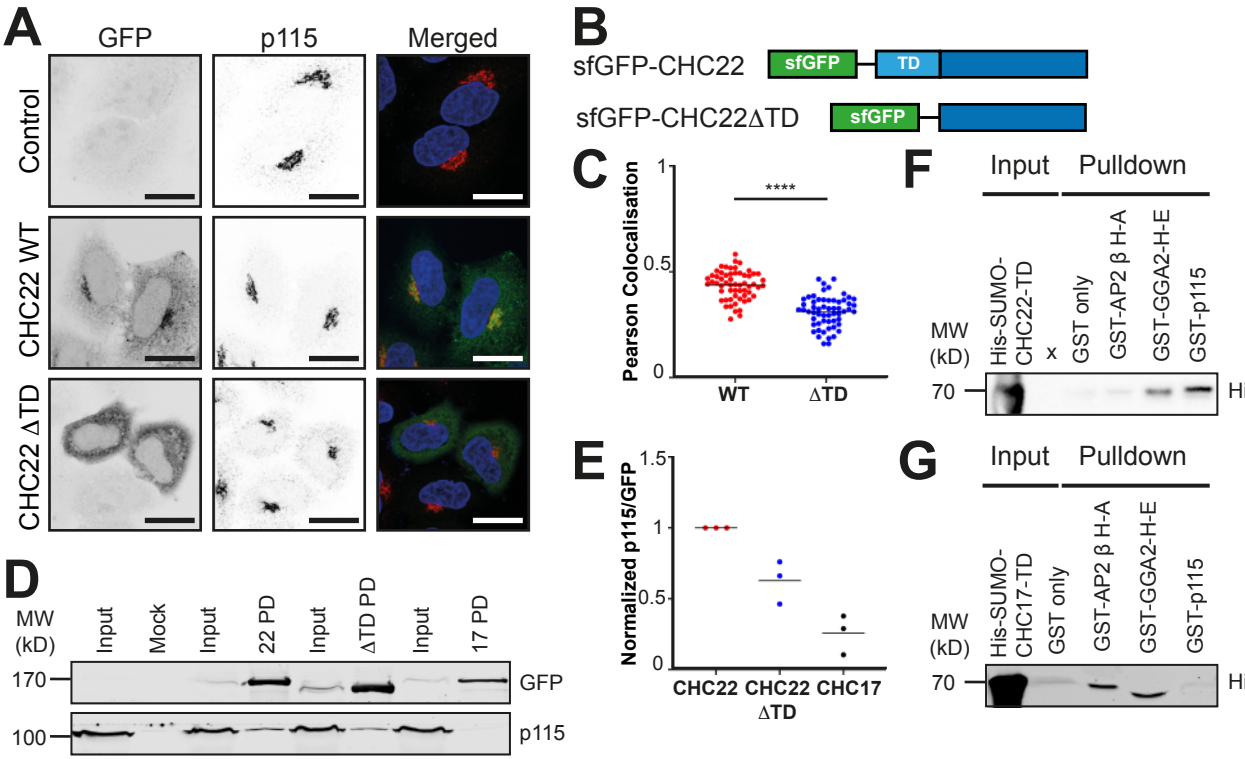
A
GFP
p115
Merged
Control
CHC22 WT
CHC22 ΔTD
B
sfGFP-CHC22
sfGFP
TD
sfGFP-CHC22ΔTD
sfGFP
C
Pearson Colocalisation
****
WT
ΔTD
D
MW (kD)
Input
Mock
Input
22 PD
Input
ΔTD PD
Input
17 PD
170
GFP
100
p115
E
Normalized p115/GFP
CHC22
CHC22 ΔTD
CHC17
F
Input
Pulldown
MW (kD)
His-SUMO-CHC22-TD
x
GST only
GST-AP2 β H-A
GST-GGA2-H-E
GST-p115
70
His
G
Input
Pulldown
MW (kD)
His-SUMO-CHC17-TD
GST only
GST-AP2 β H-A
GST-GGA2-H-E
GST-p115
70
His

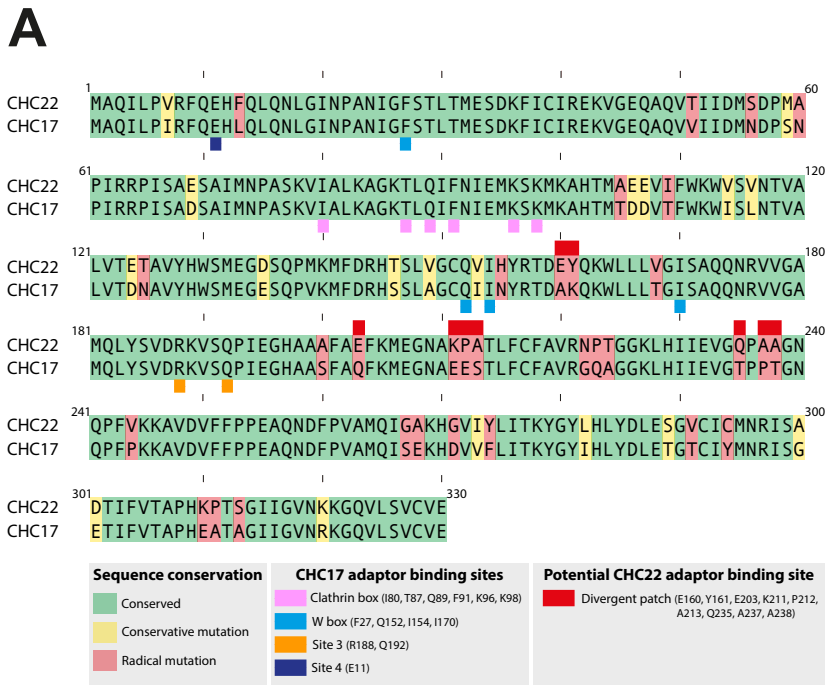
A
CHC22 1 MAQILPVRFQEHFQLQNLGINPANIGFSTLTMESDKFICIREKVGEQAQVTIIDMSDPMA 60
CHC17 MAQILPIRFQEHLQLQNLGINPANIGFSTLTMESDKFICIREKVGEQAQVVIIDMNDPSN
CHC22 61 PIRRPISAESAIMNPASKVIALKAGKTLQIFNIEMKSKMKAHTMAEEVIFWKWVSVNTVA 120
CHC17 PIRRPISADSAIMNPASKVIALKAGKTLQIFNIEMKSKMKAHTMTDDVTFWKWISLNTVA
CHC22 121 LVTETAVYHWSMEGDSQPMKMFDRHTSLVGCQVIHYRTDEYQKWLLLVGISAQQNRVVGA 180
CHC17 LVTDNAVYHWSMEGESQPVKMFDRHSSLAGCQIINYRTDAKQKWLLLTGISAQQNRVVGA
CHC22 181 MQLYSVDRKVSQPIEGHAAAFAEFKMEGNAKPATLFCFAVRNPTGGKLHIIEVGQPAAGN 240
CHC17 MQLYSVDRKVSQPIEGHAASFAQFKMEGNAEESTLFCFAVRGQAGGKLHIIEVGTPPTGN
CHC22 241 QPFVKKAVDVFFPPEAQNDFPVAMQIGAKHGVIYLITKYGYLHLYDLESGVCICMNRISA 300
CHC17 QPFPKKAVDVFFPPEAQNDFPVAMQISEKHDVVFLITKYGYIHLYDLETGTCIYMNRISG
CHC22 301 DTIFVTAPHKPTSGIIGVNKKGQVLSVCVE 330
CHC17 ETIFVTAPHEATAGIIGVNRKGQVLSVCVE
Sequence conservation
Conserved
Conservative mutation
Radical mutation
CHC17 adaptor binding sites
Clathrin box (I80, T87, Q89, F91, K96, K98)
W box (F27, Q152, I154, I170)
Site 3 (R188, Q192)
Site 4 (E11)
Potential CHC22 adaptor binding site
Divergent patch (E160, Y161, E203, K211, P212, A213, Q235, A237, A238)

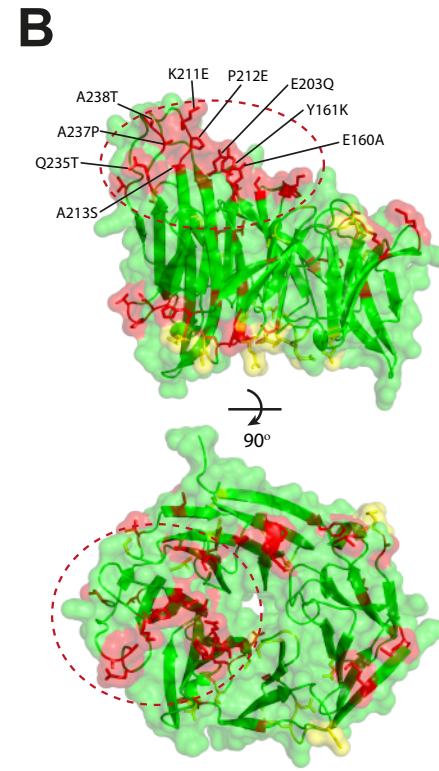
B
K211E
P212E
E203Q
A238T
Y161K
A237P
E160A
Q235T
A213S
90°

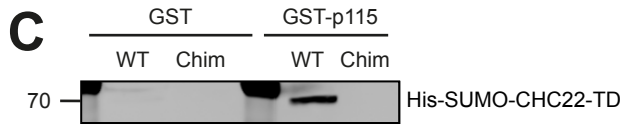
C
GST
GST-p115
WT
Chim
WT
Chim
70
His-SUMO-CHC22-TD

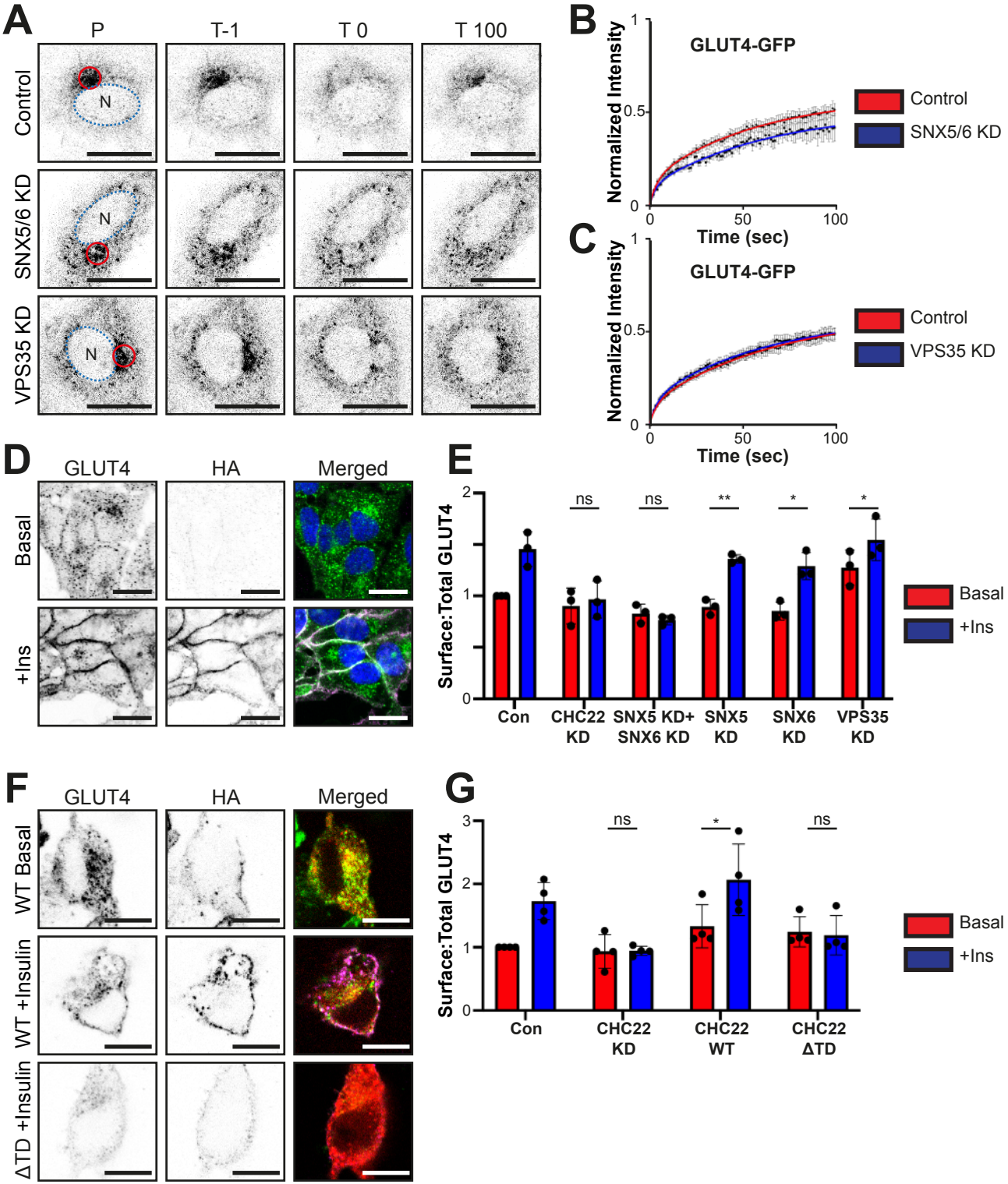
A
P
T-1
T 0
T 100
Control
SNX5/6 KD
VPS35 KD
N
B
GLUT4-GFP
Normalized Intensity
Time (sec)
Control
SNX5/6 KD
C
GLUT4-GFP
Normalized Intensity
Time (sec)
Control
VPS35 KD
D
GLUT4
HA
Merged
Basal
+Ins
E
Surface:Total GLUT4
ns
ns
**
*
*
Con
CHC22 KD
SNX5 KD+ SNX6 KD
SNX5 KD
SNX6 KD
VPS35 KD
Basal
+Ins
F
GLUT4
HA
Merged
WT Basal
WT +Insulin
ΔTD +Insulin
G
Surface:Total GLUT4
ns
*
ns
Con
CHC22 KD
CHC22 WT
CHC22 ΔTD
Basal
+Ins

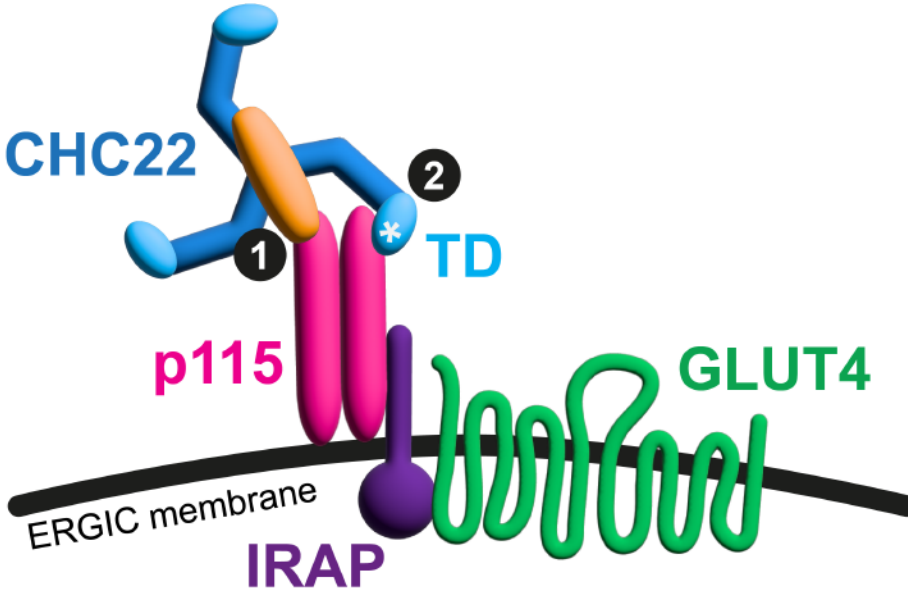
CHC22
2
1
*
TD
p115
GLUT4
ERGIC membrane
IRAP

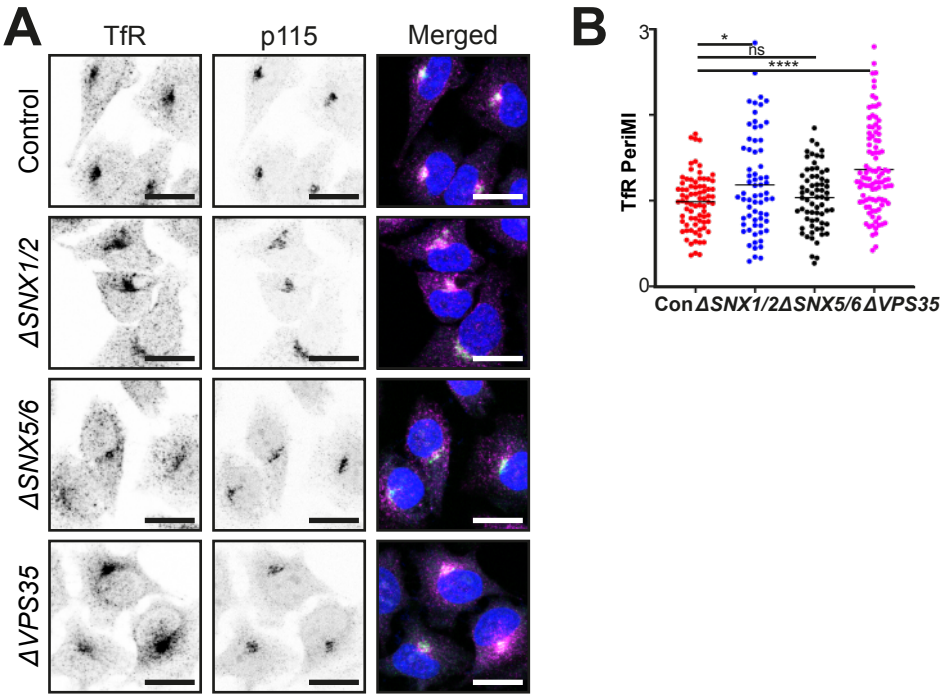
A
TfR
p115
Merged
Control
ΔSNX1/2
ΔSNX5/6
ΔVPS35
B
TfR PeriMI
3
0
*
ns
****
Con
ΔSNX1/2
ΔSNX5/6
ΔVPS35

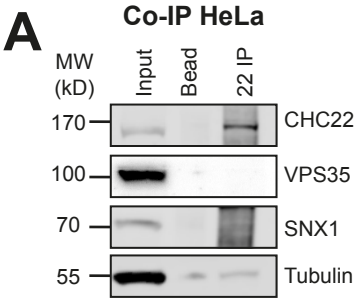
A
Co-IP HeLa
MW
(kD)
Input
Bead
22 IP
170
100
70
55
CHC22
VPS35
SNX1
Tubulin